International Journal of Robotics and Control Systems
Vol. 4, No. 2, 2024, pp. 502-535
ISSN 2775-2658
http://pubs2.ascee.org/index.php/ijrcs

Dynamic Performance Evaluation of a Brushless AC Motor Drive Using Different Sensorless Schemes

Mohamed A. El Sawy [a,1], Omar Makram Kamel [b,2], Yehia S. Mohamed [a,3], Mahmoud A. Mossa [a,4,*]

[a] Electrical Engineering Department, Faculty of Engineering, Minia University 61111, Minia, Egypt
[b] Electrical and Computer Department, Higher Institute of Engineering and Technology, El-Minia, Egypt
[1] mohammedsawi59@yahoo.com; [2] OMK@mhiet.edu.eg; [3] yehia.ali@mu.edu.eg; [4] mahmoud_a_mossa@mu.edu.eg
* Corresponding Author

ARTICLE INFO

Article history
Received January 27, 2024
Revised March 17, 2024
Accepted May 05, 2024

Keywords
Sensorless Control;
Brushless AC Motors;
Dynamic Performance;
Rotor Speed;
Estimation Error;
Response Time;
Robustness

ABSTRACT

The presented study concerns with evaluating the dynamic performance of an isotropic sinusoidal brushless motor drive while utilizing different sensorless schemes. Three estimation algorithms are considered: the first depends on extracting the speed and position via comparing two values of motor's voltage in two co-ordinate systems; the second extracts the speed and position signal via comparing two different values of motor's current defined in two co-ordinates; while the third depends on estimating the motor's flux and use it to get the speed and position. The vector control is adopted to manage the drive dynamics. The detailed mathematical derivations for all system components are presented to facilitate the performance analysis. The theoretical base of each sensorless scheme is also described in detail. The target of the provided comparative analysis is to outline the weakness and strength points of each adopted sensorless schemes while estimating the speed and rotor position for a wide operating speed range. The judgment is measured in terms of the speed and rotor position estimation errors and the dynamic response as well. The performance evaluation process is carried out using MATLAB/Simulink software in which all system parts are simulated using their mathematical models. The findings from the study state that when it comes to dynamic speed behaviour, the voltage-based sensorless technique dominates, while the current-based sensorless approach gives stability in speed estimate priority. Alternatively, the third adopted sensorless scheme offers an acceptable high-speed performance and respectable performance at lower speeds. Statistically, it is found that the voltage-based estimation technique gives respectively lower speed and position estimation errors with percentages of 35% and 10% lower than their values under the current-based estimation technique, and with percentages of 35% and 30% lower than their values under the third adopted scheme.

1. Introduction

Brushless AC motors (BLAC) such as PMSM motors are used in a wide range of industrial applications for electromechanical systems due to their high power densities, high torque-to-inertia ratio, high operating efficiency, and good control over a broad range of speeds. High performance drive systems are used in machine tools, robotics, rolling mills and other applications where they must

respond quickly and accurately, recover quickly from disturbances, and be insensitive to changes in parameters. In such applications, the PMSM can provide performance characteristics that are comparable to those of a separately excited DC motor if the vector control scheme is adopted [1]-[4]. In addition to decoupling torque and flux for quicker response, the PMSM drive system's vector control scheme also simplifies the control task. The principle of vector control stands on decoupling the flux and torque control of the machine via identifying the corresponding stator current components. The stator current is decoupled into two orthogonal components (direct and quadrature) which found that they are proportional to the motor flux and torque, respectively. The reference d-q stator currents are derived firstly using the command speed and flux values, and then compared with the actual d-q current components. Later, the current errors are fed to linear PI controllers to provide the reference voltage signals to be applied on the motor windings via a voltage source inverter (VSI). In order to satisfy the additional requirements of the high performance drive, the speed controller utilized in the PMSM drive system is crucial. It should allow the drive to track any reference speed while accounting for variations in parameters, saturation, and the impact of the load. Both dc and ac motor drives have extensively utilized conventional controllers, such as proportional integral (PI) or proportional integral differential (PID). However, designing these kinds of controllers can be challenging in the absence of a precise system model. Furthermore, the performance of these controllers for a broad range of speed operations is impacted by unrecognized load dynamics and further elements like temperature, saturation and noise [5]-[7]. These facts can be inferred to the dependency of the controllers' coefficients on the system model which can be varied under different operating conditions.

In addition to the load variation, coupling the load to the motor's shaft may result in changes in the friction coefficient and inertia. A PMSM speed control technique utilizing input-output linearization has been presented [8]-[10]. To strengthen the scheme's resistance to imprecise speed measurements, an integral controller has been added. Other variations in motor parameters, however, have not been taken into account. Even though adding an integral controller can enhance a steady-state response, it is unable to provide a good transient response when there is a parameter variation. By using nonlinear controllers, the performance of variable speed drives with PMSM can be enhanced. For electrical drives, feedback linearization has proven to be one of the most helpful control laws [11]-[13]. The main goal of this method is to apply feedback control techniques by algebraically transforming the dynamics of the nonlinear system into a completely or partially linearized system. A mechanical or optical sensor is needed to collect position and speed as part of the state that has to be fed back in order to apply feedback linearization. However, when sensorless control techniques are developed, mechanical sensors can be avoided. In these situations, it is necessary to estimate the rotor's position and speed; the control law is then calculated using these estimated values. The estimation of the speed and rotor position is a vital process as they are used for the co-ordinates transformation needed by the vector control. Any simple deviation in the angular position can result in deteriorating the dynamics of the controlled system.

BLAC motor drives have considered the proposal of several sensorless control schemes. Essentially, though, these fall into two groups: 1) those where the rotor position is determined by integration and the speed is inferred from an observer [14]-[16] and 2) those where the speed is determined by differentiation and the rotor position is inferred from an observer [17]-[22]. Nevertheless, in the first category, errors in speed, such as the integration of a constant error, may lead to inaccurate estimates of rotor position. This can make the estimate of rotor position unreliable if a suitable compensating technique is not used. In the second category, noise will also be amplified and result in errors in the estimated speed if the speed is solely determined by the differential of the rotor position [19], [20]. The study in [23] suggested that the flux vector be preprocessed with a low-pass filter to improve the accuracy of the derived position signal so that it can be differentiated for the estimation of speed when the rotor position is determined directly from the observed flux vector. On the other hand, applying a low-pass filter in a variable-speed BLAC drive will typically cause the fundamental flux vector to shift phase across a large frequency range. Since the average speed method provides the accurate value when the motor is operating at steady state, it is therefore more commonly

used. However, its dynamic response is typically too slow; therefore it is not typically utilized for speed feedback in servo systems. A different method, which has been suggested in [17], [18], [24], is to calculate the speed using the excitation flux linkage to the induced electromotive force (EMF) ratio. Although this speed estimation method responds quickly, it has two major shortcomings. Firstly, the current differential is needed to calculate the EMF. As a result, noise has the potential to introduce a large speed error. Although the differential was no longer necessary as proposed in [25], [26], this led to a much more intricate control system architecture. By contrast, the study in [27] assumed that the current was constant and that its differential was zero at the end of each flux observing step. Nonetheless, this kind of assumption is generally incorrect. Second, factors that affect the estimated speed, like temperature and saturation variations, might alter parameters like the excitation flux linkage, inductance, and resistance. As a result, the study [27] also used the estimated average speed as the compensation reference (i.e., input variable) to account for parameter fluctuations. Nevertheless, it is challenging to adjust for differences in three parameters using just one input variable.

As stated earlier, PMSM rotor position and speed can be estimated using state observers. A state observer or state estimator in control theory is a system that, using measurements of the real system's input and output, produces an estimate of the internal state of a particular real system. Many control theory tasks, such as stabilizing a system using state feedback, require knowledge of the system state. In most real-world situations, it is impossible to ascertain the system's physical condition from direct observation. Rather, the system outputs allow for the observation of the internal state's indirect impacts. A number of methods have been put forth to obtain PMSM state observers, including extended Kalman filter (EKF), viz. nonlinear observers, nonlinear reduced order observers, and nonlinear full order observers based on linearization [28]. Speed controllers based on observers have been proposed in [28]-[31]. In order to design the observer-based controller in these papers, some presumptions must be introduced. In [29], a known load torque has been taken into account, whereas in [30], the controller is designed with the assumption that the inductance is zero. The authors of [28] make the assumption that the machine's speed is roughly constant over a brief period of time (sampling interval). However, mismatches resulting from an unknown load torque, a nonzero inductance, and variable speed must be compensated for when higher performance is needed. Two new methods for controlling the speed of the PMSM have been reported recently: one is adaptive input-output linearization [32]-[34], and the other is sliding mode control [35]-[37]. Notwithstanding the possibility of achieving good performance, the controller design is fairly intricate.

Despite the plethora of studies on sensorless schemes for estimating speed and rotor position, a noticeable gap exists in the literature regarding comparative analyses of multiple estimation systems. This paper aims to address this gap by conducting a thorough comparative study, evaluating the performance of different sensorless schemes used with the brushless AC motor drive. The importance of such a comprehensive comparison lies in identifying the schemes that yield the most accurate estimations, minimizing deviations between estimated and actual variables.

In summary, this paper navigates through the landscape of motor control systems, shedding light on the intricacies of sensorless techniques for brushless synchronous motors. Through a meticulous comparative analysis, the goal is to uncover the most effective sensorless schemes, providing valuable insights for optimizing motor control in diverse applications. The contributions that the study introduces are itemized as following:

- The paper investigates the dynamic behavior of a brushless AC motor drive when considering three different sensorless schemes.
- The detailed modeling and description for the control system and the adopted sensorless scheme is presented and analyzed.
- The performed comparative study enabled the identification of the strength and weakness points of each sensorless scheme.

- The study revealed that three sensorless schemes can be merged to exploit the advantages of each one and to obtain better estimation.
- The presented study can be extended to be considered with other types of AC machine drives after considering the theory of operation of each type.

The structure of the paper comes in the following form: Section 2 introduces the system modeling including the PMSM model, inverter model and the adopted vector control. Section 3 introduces a detailed theoretical analysis for the sensorless schemes under investigation. Afterwards, the drive performance under each sensorless technique is evaluated and presented in Section 3. A comparative analysis is also introduced in this section. Finally, Section 5 outlines the conclusions of the study.

2. System Modeling

2.1. Model of BLAC Motor

The equivalent circuit captures the essential components of the PMSM, including the stator windings, rotor, and magnetic field. Sequentially numbered equations illustrate the interrelation between the electrical and mechanical aspects of the motor. The equivalent circuit of the PMSM model is illustrated in Fig. 1 [6].

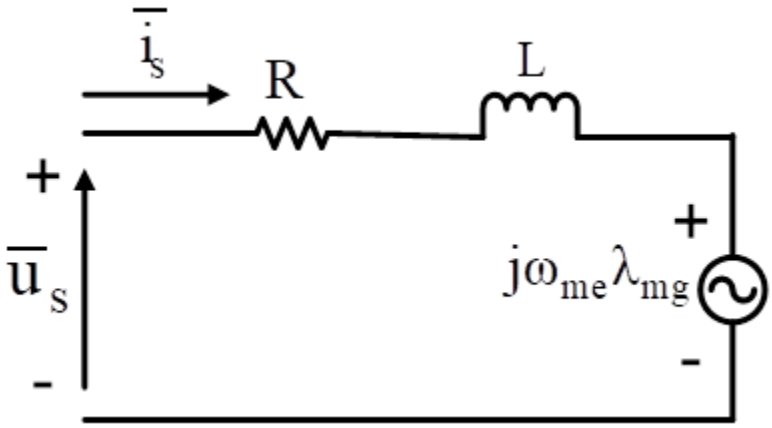

Fig. 1. PMSM equivalent circuit

The dynamic of electric sub-model of the PMSM can be described using the following mathematical relationships:

$$pi_{ds} = \frac{1}{L}(u_{ds} - Ri_{ds} + \Lambda_{qs}\omega_{me}) \quad (1)$$

$$pi_{qs} = \frac{1}{L}(u_{qs} - Ri_{qs} - \Lambda_{ds}\omega_{me}) \quad (2)$$

where Λ_{ds} and Λ_{qs} are the d-q components of stator flux and they are calculated by.

$$\Lambda_{ds} = Li_{ds} + \lambda_{mg} \quad \text{and} \quad \Lambda_{qs} = Li_{qs} \quad (3)$$

where R and L are the resistance and inductance of the stator windings, and λ_{mg} is the rotor magnet. p denotes to the differential operator (d/dt). Alternatively, the dynamic of the mechanical sub-model can be expressed by.

$$p\omega_{me} = \frac{1}{J_m}(T_e - T_l - F\omega_{me}) \quad (4)$$

where T_l is the load torque, J_m is the inertia, F is the rotor friction and T_e is the developed torque for an isotropic PMSM is defined by.

$$T_e = 1.5P\Lambda_{mg}i_{qs} \tag{5}$$

2.2. Model of VSI

Three-phase counterparts of the full bridge voltage source inverters are shown in Fig. 2. The main purpose of this topology is to provide a three-phase voltage source, where the amplitude, phase and frequency of the voltages can be controlled. The standard three-phase inverter shown in Fig. 2 has six switches the switching of which depends on the modulation scheme. The input dc is usually obtained from a single-phase or three phase utility power supply through a diode-bridge rectifier and LC or C filter.

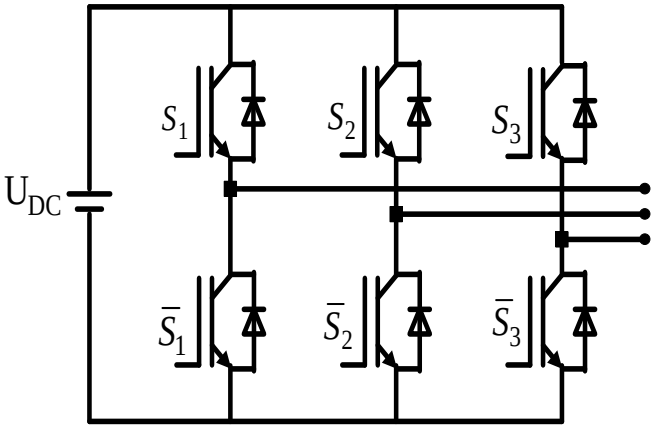

Fig. 2. Three-phase inverter

A single function can be used to mathematically represent the inverter's potential switching states as follows [38]:

$$S = \frac{2}{3}(S_1 + aS_2 + a^2S_3) \tag{6}$$

where the on/off switching actions of the upper and lower switches are represented by $S_{i,1,2,3}$ and $\bar{S}_{i,1,2,3}$, respectively, and $a = e^{j\frac{2\pi}{3}}$. After determining the switching state S, the stator voltage is computed using the DC link voltage U_{dc} as.

$$\bar{u}_s = SU_{dc} \tag{7}$$

2.3. Control System Modeling

The schematic diagram of the vector control used for the PMSM is illustrated in Fig. 3. As shown the main idea behind this control is the total alignment of the permanent magnet flux with the direct axis of the stator, so that the following relationship can be achieved.

$$\Lambda_{ds} = \lambda_{mg} \tag{8}$$

The above relationship is realized via maintaining the value of i_{ds} equals zero. This action is usually used to prevent weakening the permanent flux value to keep the excitation inside the machine with the appropriate rate.

Accordingly the torque can be directly regulated via controlling the q-axis stator current i_{qs} according to the following relationship.

$$T_e = 1.5P\lambda_{mg}i_{qs} \tag{9}$$

It is noted that, there is a need for precise identification for both the speed ω_{me} and position θ_{me} of the rotor to ensure correct transformation between different co-ordinates. Accordingly selecting the appropriate sensorless scheme is a vital step to be accomplished.

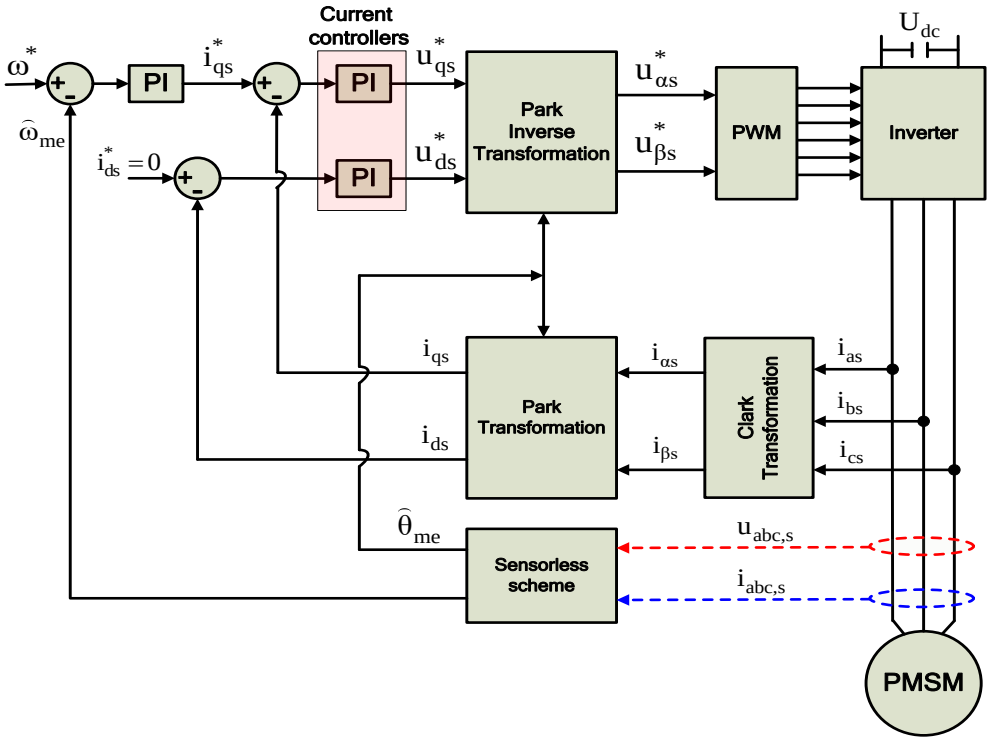

Fig. 3. Schematic of vector control for PMSM

The tuning of PI current controllers shown in Fig. 3 can be analyzed mathematically as following: By formulating Equations (1) and (2), this gives.

$$u_{ds} = (\overbrace{Ri_{ds} + L\frac{di_{ds}}{dt}}^{active\ term} - \overbrace{L\omega_{me}i_{qs}}^{compensating\ term}) \tag{10}$$

$$u_{qs} = \overbrace{Ri_{qs} + L\frac{di_{qs}}{dt}}^{active\ term} + \overbrace{L\omega_{me}i_{ds} + \omega_{me}\lambda_{mg}}^{compensating\ term} \tag{11}$$

While the active terms are used to drive the transfer function, which determines how the stator voltage will react to changes in the stator current, and achieve the desired change in the stator current, the compensatory terms are used to lessen disturbances. The Laplace transform is then applied to the active terms, which results in.

$$u_{ds}(s) = (sL + R)i_{ds}(s) \quad \text{and} \quad u_{qs}(s) = (sL + R)i_{qs}(s) \tag{12}$$

Then, by reformulating, it gives.

$$\frac{i_{ds}(s)}{u_{ds}(s)} = \frac{1}{SL + R} \tag{13}$$

$$\frac{i_{qs}(s)}{u_{qs}(s)} = \frac{1}{SL+R} \tag{14}$$

Moreover, the transfer function of the PI stator current regulators is represented by.

$$k_p + \frac{K_i}{s} = (i^*_{ds}(s) - i_{ds}(s)) \tag{15}$$

$$k_p + \frac{K_i}{s} = (i^*_{qs}(s) - i_{qs}(s)) \tag{16}$$

Then, we obtained the following by dividing the two sides of Equations (15) and (16) respectively on $i_{ds}(s)$ and $i_{qs}(s)$, it gives.

$$\frac{u_{ds}(s)}{i_{ds}(s)} = (\frac{sK_p + K_i}{s})[\frac{i^*_{ds}(s)}{i_{ds}(s)} - 1] \tag{17}$$

$$\frac{u_{qs}(s)}{i_{qs}(s)} = (\frac{sK_p + K_i}{s})[\frac{i^*_{qs}(s)}{i_{qs}(s)} - 1] \tag{18}$$

The following formula can be then obtained by substituting the voltage components $u_{ds}(s)$ and $u_{qs}(s)$ from Equation (12), it results in.

$$(sL + R) = (\frac{sK_p + K_i}{s})[\frac{i^*_{ds}(s)}{i_{ds}(s)} - 1] \tag{19}$$

$$(sL + R) = (\frac{sK_p + K_i}{s})[\frac{i^*_{qs}(s)}{i_{qs}(s)} - 1] \tag{20}$$

After some manipulations, the following is obtained.

$$\frac{i_{ds}(s)}{i^*_{ds}(s)} = \frac{sK_p+K_i}{s^2L+s(R+K_p)+K_i} \text{ and } \frac{i_{qs}(s)}{i^*_{qs}(s)} = \frac{sK_p+K_i}{s^2L+s(R+K_p)+K_i} \tag{21}$$

The denominator of equations (21) represents the characteristic equation guiding the dynamics of the PI current regulators; this equation must have negative real roots in order for the system to stay stable. Accordingly,

$$s^2L + s(R + K_p) + K_i = 0 \tag{22}$$

Alternatively, the second order dynamic system's formula can be defined by.

$$s^2 + 2\zeta w_n s + w_n^2 = 0.0 \tag{23}$$

where ζ is the damping ratio and w_n is the natural frequency.

Now and by comparing Equations (22) and (23), the coefficients of the PI current regulators are calculated by.

$$K_p = 2\zeta w_n L - R \quad \text{and} \quad K_i = w_n^2 L \tag{24}$$

3. Adopted Sensorless Schemes

In this paper, in-depth exploration is undertaken on three sensorless drives designed for sinusoidal and isotropic brushless motors, as N. Matsui and G.R. Selmon proposed in the referenced

articles [17], [18], [39]-[41]. These methods are pivotal in accurately estimating the speed and position of the rotor, crucial parameters for the effective operation of this particular electric machine.

It's important to note that the scope of this study on sensorless algorithms is primarily focused on the operational aspects of the motor under steady-state conditions. It does not delve into the challenges associated with motor startup or the determination of the initial rotor position, focusing exclusively on the motor's performance during ongoing operation, thereby omitting the unique issues that arise during the initial moments of operation.

3.1. First Sensorless Categorization

This method was initially introduced by Matsui [18] and has been utilized to develop sensorless control systems for various sinusoidal brushless motors, further applied and discussed in several articles [17], [39], [40].

Matsui's ingenious approach enables the operation of these motors without the reliance on encoders or resolvers. Instead, it derives a signal that is proportionate to the angular position and speed by comparing two reference systems: one real and one hypothetical. Two distinct planes are available, based on the parameter chosen for comparison. The first approach involves analyzing voltages [18], while the second method utilizes the motor's phase currents [39]. Matsui has also assessed and compared the performance of these methods in [17], including their integration with motor parameter estimation algorithms in [40].

3.1.1. Voltage Based Technique

As illustrated in Fig. 4. The model introduces two reference systems, namely the d-q and γ-δ axes. The d-q axes, commonly defining the actual rotor position, align the d-axis with the magnetic flux vector created by the permanent magnets (λ_{mg}). In contrast, the γ-δ axes represent a hypothetical coordinate system within the controller, introducing an angular difference Δθ between the two reference systems.

$$\Delta\theta = \theta_c - \theta_{me} \tag{25}$$

Here, θ_{me} denotes the real electromechanical position, and θ_c is the estimated position within the controller.

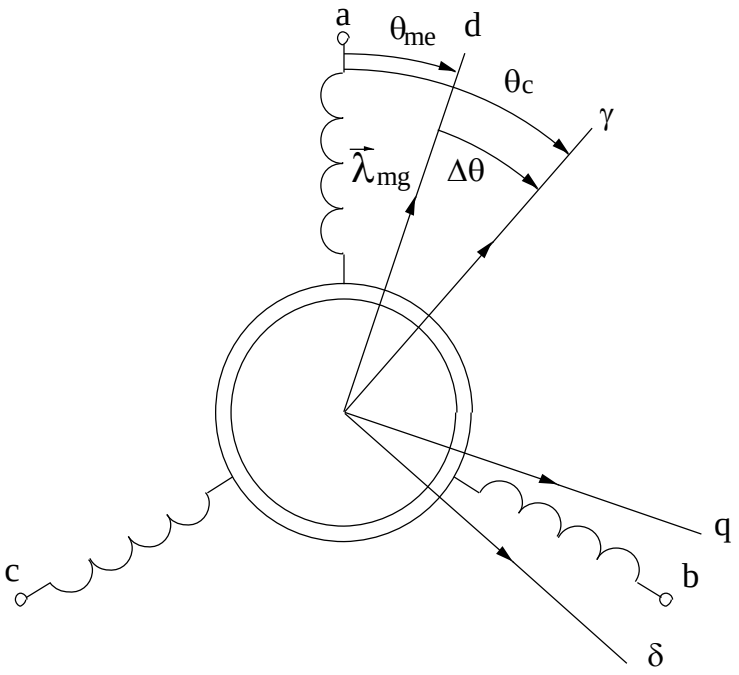

Fig. 4. Actual and hypothetical co-ordinations

By utilizing the T_{abc}/T_{dq} matrix, voltages and currents can be transformed into the d-q reference system. In sensorless drives, where the rotor position is unknown, the same matrix can still be applied by incorporating θ_c instead of the actual angular reference (θ_{me}).

$$\begin{bmatrix}\gamma\\ \delta\end{bmatrix} = \overbrace{\frac{2}{3}\begin{bmatrix} cos(\theta_c) & cos(\theta_c - 2\pi/3) & cos(\theta_c + 2\pi/3) \\ -sin(\theta_c) & -sin(\theta_c - 2\pi/3) & -sin(\theta_c + 2\pi/3)\end{bmatrix}}^{T_{abc}/T_{dq}} \times \begin{bmatrix}a\\ b\\ c\end{bmatrix} \tag{26}$$

In conventional drives, the angular reference is typically provided by an encoder, allowing for voltage equation derivation in the γ-δ coordinate system:

$$\begin{bmatrix}u_\gamma\\ u_\delta\end{bmatrix} = \begin{bmatrix}R + pL & -L\omega_c \\ L\omega_c & R + pL\end{bmatrix}\begin{bmatrix}i_\gamma\\ i_\delta\end{bmatrix} + \Lambda_{mg}\omega_{me}\begin{bmatrix}-sin\,(\Delta\theta)\\ cos\,(\Delta\theta)\end{bmatrix} \tag{27}$$

Estimating rotor position and speed is achieved by assuming ideal conditions ($\Delta\theta = 0$ and $\omega_c = \omega_{me}$), resulting in Equation (28):

$$\begin{bmatrix}u_{\gamma M}\\ u_{\delta M}\end{bmatrix} = \begin{bmatrix}R + pL & -L\omega_c \\ L\omega_c & R + pL\end{bmatrix}\begin{bmatrix}i_\gamma\\ i_\delta\end{bmatrix} + \Lambda_{mg}\omega_{me}\begin{bmatrix}0\\ 1\end{bmatrix} \tag{28}$$

These expressions represent the voltage equations in the system reference d-q, assuming no difference between the two reference systems. However, these values are theoretical and cannot be directly measured but are calculable. The actual currents transformed into γ-δ and the estimated speed are utilized to calculate the voltage difference Δu_γ for the actual and estimated components of the γ-axis using Equation (29):

$$\Delta u_\gamma = u_\gamma - u_{\gamma M} = \Lambda_{mg}\,\omega_{me}\;sin\,(\Delta\theta) \tag{29}$$

Here, u_γ and $u_{\gamma M}$ represent the actual and estimated voltage components of the γ-axis, espectively.

Assuming $\omega_{me} \neq 0$ and $\Delta\theta \approx 0$, Equation (30) approximates $\Delta u_\gamma \propto \Delta\theta$. This equation demonstrates that the phase shift between the real and hypothetical reference systems can be estimated through a voltage difference, enabling a practical implementation within a suitable controller. Notably, this estimation can be achieved by measuring motor currents, minimizing the need for additional transducers.

$$\Delta u_\gamma = u_\gamma - u_{\gamma M} \propto \Delta\theta \tag{30}$$

It is important to note that real voltages applied to the motor can be computed by considering the DC voltage applied to the inverter input, PWM values, and information on dead times. Therefore, the angular difference can potentially be estimated by measuring only the motor currents, reducing the need for additional transducers.

Once the estimation of the difference $\Delta\theta$ is accomplished, the next step is to synchronize the two axes. This involves either increasing the rotational speed of the hypothetical axis when $\Delta\theta < 0$ or decreasing it when $\Delta\theta > 0$. The synchronization process is illustrated in Fig. 5.

To achieve this synchronization, it is crucial to determine and subsequently estimate the rotational speed of the reference system, especially in the absence of sensors for direct measurement. This estimation can be derived easily from the δ component of Equation (28):

$$\omega_{me} = \frac{u_\delta - (R + Lp)i_\delta}{\lambda_{mg} + Li_\gamma} \tag{31}$$

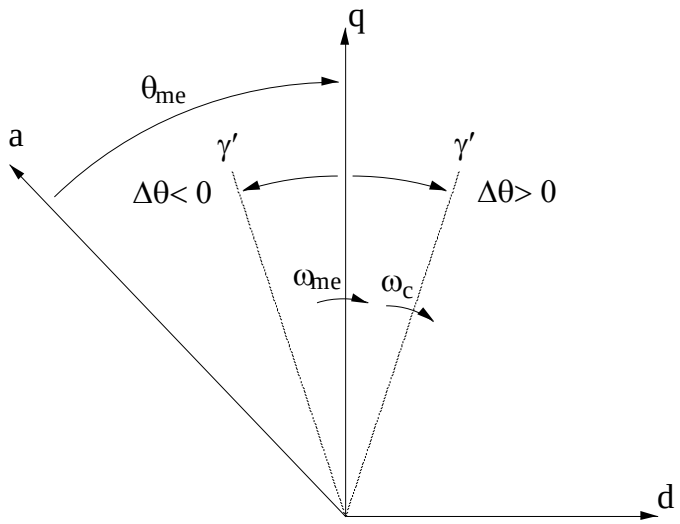

Fig. 5. Explanation of the mechanism of self-synchronization

Since the angular position is the integral of speed, the difference $\Delta\theta$ can be nullified by appropriately adjusting the parameter α, referred to as "speed correction." This parameter represents the difference between the speed of the hypothetical system and the estimated speed required for the actual system to rotate.

$$\alpha = \omega_c - \omega_{me} \tag{32}$$

Based on these considerations, an algorithm can be devised to act on α and drive $\Delta\theta$ towards zero in the case of counterclockwise rotation or clockwise rotation. Accordingly, the algorithm can be defined as:

$$\begin{aligned} &\text{counterclockwise} \begin{cases} if\ \Delta\theta > 0\ (\Delta u_\gamma > 0), then\ \alpha\ < 0 \\ if\ \Delta\theta < 0\ (\Delta u_\gamma < 0), then\ \alpha > 0 \end{cases} \\ &\text{clockwise} \quad\ \begin{cases} if\ \Delta\theta > 0\ (\Delta u_\gamma > 0), then\ \alpha > 0 \\ if\ \Delta\theta < 0\ (\Delta u_\gamma < 0), then\ \alpha < 0 \end{cases} \end{aligned} \tag{33}$$

There are various ways to implement and obtain the corrective parameter α. This study employs a straightforward implementation using a PI-type controller:

$$\alpha = -\left(K_{SP}\Delta u_\gamma + K_{SI}\int \Delta u_\gamma dt\right) sgn(\omega_c) \tag{34}$$

Here, K_{SP} and K_{SI} are the controller gains. By using the α parameter, the rotor speed can be obtained by correcting the estimation fairly as following.

$$\omega_c = \omega_{me} + \alpha \tag{35}$$

The methodology for sensorless control unfolds through a systematic series of steps. Starting with the measurement of three-phase currents, the voltages are obtained either through sensors or calculations based on measured currents to enhance cost-effectiveness. Both currents and voltages undergo a coordinate transformation into the γ-δ reference system.

Then, rotor speed estimation is performed using Equation (31) using transformed currents and voltages, is followed by determining hypothetical voltages through Equation (28), Actual motor voltages are known. The angular difference $\Delta\theta$ between real and hypothetical reference systems is then calculated with Equation (30). Assuming an estimated motor speed (ω_{me}) is not zero and $\Delta\theta$ is approximately zero, the approximation $\Delta u_\gamma \propto \Delta\theta$ is made.

The speed correction parameter α is calculated using Equation (34), incorporating proportional and integral terms. The estimated speed ω_c is modified according to Equation (35). This estimated speed is compared with the speed reference ω^*, and any difference ($\Delta\omega$) becomes the input to a Proportional-Integral (PI) regulator. The output of this regulator serves as the reference current i_δ^*, which, upon comparison with actual motor currents transformed into the γ-δ reference system, generates signals for motor control. Fig. 6 illustrates the complete system diagram for the adopted sensorless technique.

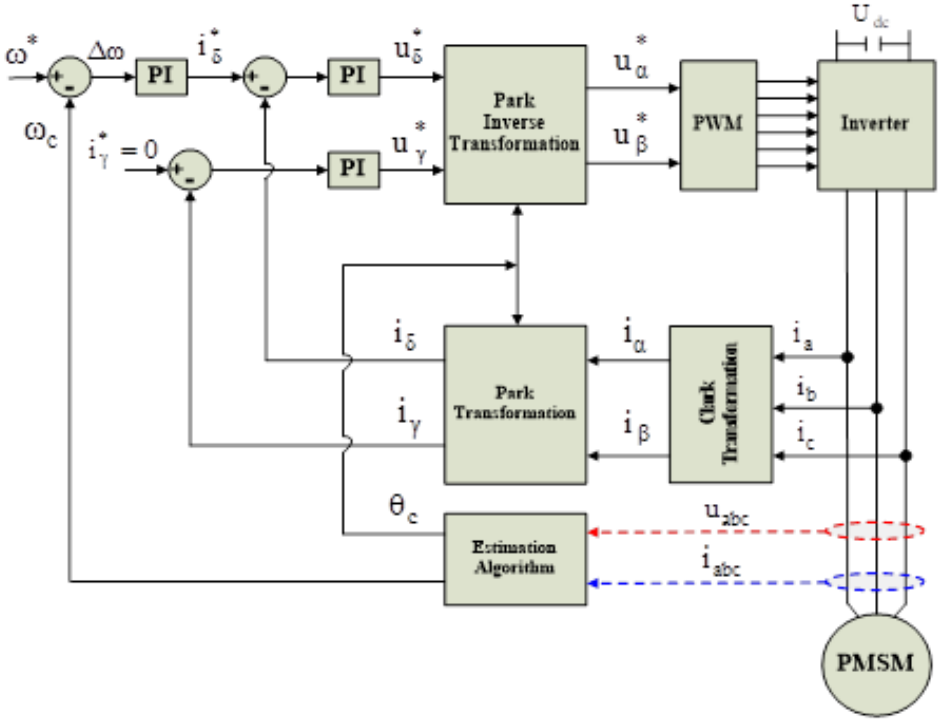

Fig. 6. Schematic diagram of voltage based sensorless technique for PMSM

3.1.2. Current Based Technique

Building upon the sensorless drive algorithm discussed in Sec. 3.1.1, a variant introduced by [17], [39] refines the approach. In this variant, the speed signal is derived by comparing currents instead of voltages. Notably, it retains the fundamental concept of the two reference systems that define the previously introduced version, adding a small difference to the sensorless drive implementation.

Based on the considerations made in the previous variant (voltage vector), the algorithm compares the "real" current in the d-q axes with the current obtained by solving the motor model equations in the γ-δ axes, with the controller utilizing the estimated speed rather than the actual speed.

Considering the equations derived from a simplified model of the motor, the currents are obtained by solving the model equations for a sinusoidal brushless motor. Accordingly, the dynamics of the hypothetical $\gamma - \delta$ current components can be expressed as following.

$$p\begin{bmatrix} i_\gamma \\ i_\delta \end{bmatrix} = \frac{1}{L}\left[\begin{bmatrix} u_\gamma \\ u_\delta \end{bmatrix} - \begin{bmatrix} R & -L\omega_c \\ L\omega_c & R \end{bmatrix}\begin{bmatrix} i_\gamma \\ i_\delta \end{bmatrix} - \Lambda_{mg}\omega_{me}\begin{bmatrix} -\sin(\Delta\theta) \\ \cos(\Delta\theta) \end{bmatrix}\right] \quad (36)$$

$$p\begin{bmatrix} i_\gamma \\ i_\delta \end{bmatrix} = \frac{1}{L}\left[\begin{bmatrix} u_\gamma \\ u_\delta \end{bmatrix} - \begin{bmatrix} R & -L\omega_c \\ L\omega_c & R \end{bmatrix}\begin{bmatrix} i_\gamma \\ i_\delta \end{bmatrix} - e\begin{bmatrix} -\sin(\Delta\theta) \\ \cos(\Delta\theta) \end{bmatrix}\right] \quad (37)$$

Here, e represents the electromotive force ($e = \Lambda_{mg}\omega_{me}$).

Assuming that at each sampling instant the currents are i_γ^n and i_δ^n, then at the next instant, i_γ^{n+1} and i_δ^{n+1} will be approximately given by the following relation:

The exact value of δ depends on the control algorithm or model specifics. Assuming currents at each sampling instant are i_γ^n and i_δ^n, the subsequent currents i_γ^{n+1} and i_δ^{n+1} are approximately given by:

$$\begin{bmatrix} i_\gamma^{n+1} \\ i_\delta^{n+1} \end{bmatrix} = \begin{bmatrix} i_\gamma^n \\ i_\delta^n \end{bmatrix} + p \begin{bmatrix} i_\gamma \\ i_\delta \end{bmatrix} T \tag{38}$$

Assuming the sampling period (T) is significantly smaller than the time constants of the stator currents, equations are formulated specifically for the real reference system within the controller. A key assumption is the alignment of the two reference systems (d-q system and γ-δ system), with no angular difference ($\Delta\theta = 0$) and identical angular velocity ($\omega_c = \omega_{me}$). Consequently, equations (37) and (38) transform to:

$$p \begin{bmatrix} i_{\gamma M} \\ i_{\delta M} \end{bmatrix} = \frac{1}{L} \left[\begin{bmatrix} u_\gamma \\ u_\delta \end{bmatrix} - \begin{bmatrix} R & -L\omega_c \\ L\omega_c & R \end{bmatrix} \begin{bmatrix} i_\gamma \\ i_\delta \end{bmatrix} - \mathrm{e}_c \begin{bmatrix} 0 \\ 1 \end{bmatrix} \right] \tag{39}$$

$$\begin{bmatrix} i_{\gamma\mathrm{M}}^{n+1} \\ i_{\delta\mathrm{M}}^{n+1} \end{bmatrix} = \begin{bmatrix} i_\gamma^n \\ i_\delta^n \end{bmatrix} + p \begin{bmatrix} i_\gamma \\ i_\delta \end{bmatrix} T \tag{40}$$

Here, e_c signifies the electromotive force of the motor within the new system reference. The sensorless algorithm acquires the crucial speed signal by comparing currents within the two distinct reference systems employed by the algorithm.

The error between actual motor currents and those calculated using the equations is determined by comparing equations (38) and (40). Under a simplifying assumption and considering that the sampling period (T) is small, the following approximations are made:

$$sin(\Delta\theta) \approx \Delta\theta \qquad \cos(\Delta\theta) \approx 1 \tag{41}$$

With this simplification, the current error is expressed as:

$$\begin{bmatrix} \Delta i_{\gamma\mathrm{M}}^{n+1} \\ \Delta i_{\delta\mathrm{M}}^{n+1} \end{bmatrix} = \begin{bmatrix} i_\gamma^{n+1} - i_{\gamma\mathrm{M}}^{n+1} \\ i_\delta^{n+1} - i_{\delta\mathrm{M}}^{n+1} \end{bmatrix} = \frac{T}{L} \begin{bmatrix} e.\Delta\theta \\ -(e - e_c) \end{bmatrix} \tag{42}$$

Two essential conclusions are derived from examining equation (42):The error in current on the δ axis is proportionate to the difference between the counter-electromotive force (c.e.m.f) of the model (γ-δ axes) and the actual ones (d-q axes), which can be obtained using the current error on the δ axis:

$$e_c^{n+1} = e_{cn} - K_e \cdot \Delta i_\delta^n \tag{43}$$

The error in current on the γ axis is proportionate to the angular error $\Delta\theta$ which is defined by equation (25). Thus, the electromechanical position can be determined as:

$$\theta_c^{n+1} = \theta_{cn} + \frac{e_c^{n+1}}{\lambda_{mg}} T + K_\theta \cdot \Delta i_\gamma^n \tag{44}$$

Since speed is the derivative of angular position, it is obtained using:

$$\omega_c^{n+1} = \frac{\theta_c^{n+1} - \theta_c^n}{T} = \frac{e_c^{n+1}}{\lambda_{mg}} + \frac{K_\theta}{T} \cdot \Delta i_\gamma^n \tag{45}$$

In these formulas, K_e and K_θ are gains, and their values are adjusted to achieve desired outcomes. Both voltage and current differences play a crucial role in resolving the sensorless drive problem. Notably, this method offers the advantage of using less voltage, effectively mitigating uncertainty caused by the inverter.

Fig. 7 abbreviate the systematic implementation of the current based sensorless scheme described in this section. As can be noticed, two different current signals are captured (measured and estimated) and then compared and the deviation is fed to the estimation algorithm, from which the estimated speed and position are obtained.

The outlined configuration in Fig. 7 includes measuring three-phase currents, calculating three-phase voltages, transforming these values into the γ-δ reference system, and computing hypothetical motor currents based on equations (39) and (40). Subsequent computations involve determining the counter-electromotive force (e_c^{n+1}), angular position (θ_c^{n+1}), and speed (ω_c) using previously introduced equations.

The process continues by comparing the calculated speed (ω_c) with the speed reference (ω^*). The resulting speed error ($\Delta\omega = \omega^* - \omega_c$) serves as the input to a PI regulator, generating the reference current i_δ^*. Further, the current references are compared with the real motor currents, previously transformed into the γ-δ reference system, and are utilized to generate signals sent to the inverter.

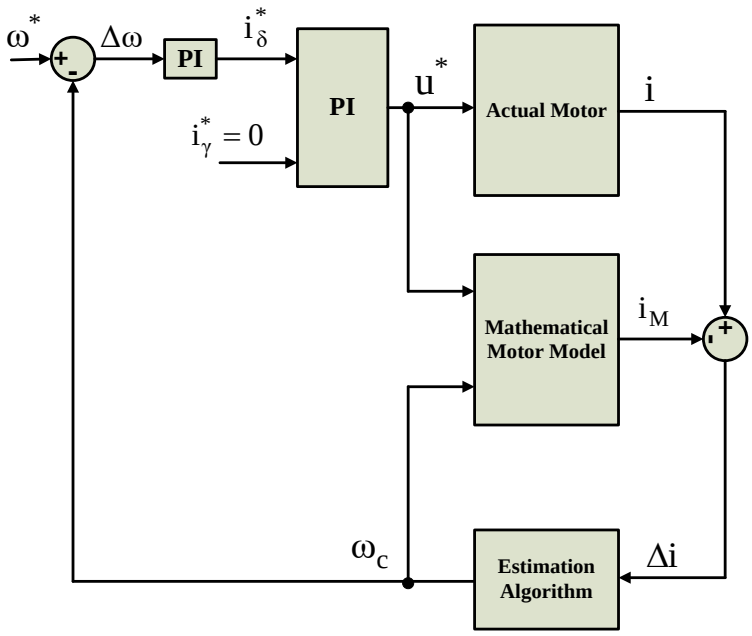

Fig. 7. System configuration of current based sensorless technique for PMSM

3.2. Second Sensorless Categorization

By exploring the operational strategy for a sinusoidal brushless sensorless motor, proposed in [41], an innovative approach reveals. This method involves examining the voltages across different motor sections and monitoring electric currents within it.

The authors introduce the concept of the space vector of the linkage flux, determined by these voltages, and utilize its angle to regulate motor power consumption. While their technique demonstrates effective performance in conducted tests, it is essential to note that its efficacy is constrained to speeds up to approximately 1Hz. Below this threshold, challenges arise due to certain electrical complexities that hinder accurate flux determination. Despite this limitation, the method remains suitable for a diverse range of speeds.

Slemon devised the flux estimation algorithm to determine rotor speed and position by analyzing the magnetic flux. That involves a thorough examination of voltages and currents within the motor to deduce the linkage flux, subsequently integrated over time to obtain the stator flux.

Establishing the angular position of the flux vector is a crucial aspect and the key parameter for sensorless control. The angle is computed using the real and imaginary components of the flux vector. Embedded within a control scheme comprising two loops—an outer speed loop and an inner current loop—the algorithm utilizes the calculated speed to control the motor, while the current loop compares actual motor currents with reference currents.

Despite facing challenges, such as resistive drops and noise amplification at lower speeds, this method facilitates extensive motor control without the need for encoders, rendering it a valuable tool for a wide range of applications. The process begins with the vector diagram of the machine, as illustrated in Fig. 8. As known, the voltage balance of the motor is defined by.

$$\bar{u}_s = R\bar{\imath}_s + \bar{e}_s = R\bar{\imath}_s + \frac{d}{dt}\bar{\lambda}_s \tag{46}$$

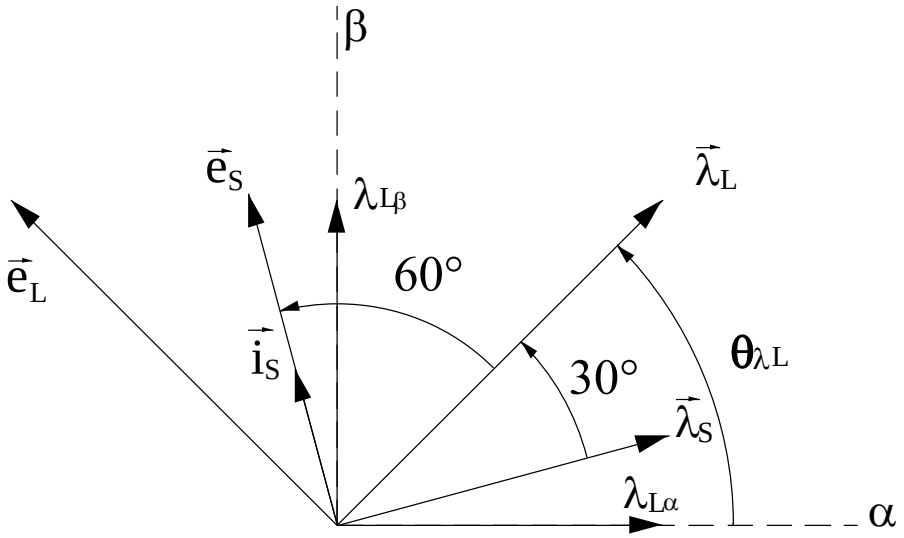

Fig. 8. Vector diagram of the brushless motor

This equation involves the stator voltage $\bar{u}_s$, stator current $\bar{\imath}_s$, and the stator flux $\bar{\lambda}_s$. By integrating the space vector of the stator's electromotive force $\bar{e}_s$, the stator flux $\bar{\lambda}_s$, the angular position of the flux vector $\theta_{\lambda L}$, and the corresponding speed $\omega_{\lambda L}$ are determined as following:

$$\bar{\lambda}_s = \int_0^t \bar{e}_s dt = \int_0^t (\bar{u}_s - R\bar{\imath}_s) dt \tag{47}$$

$$\theta_{\lambda_L} = \tan^{-1}\left(\frac{\lambda_{L\beta}}{\lambda_{L\alpha}}\right) \tag{48}$$

$$\omega_{\lambda_L} = \frac{\Delta\theta_{\lambda_L}}{\Delta t} \tag{49}$$

The flux vector λ_L is obtained by integrating the electromotive force.

$$\lambda_L = \int \bar{e}_L \, dt = \lambda_{L\alpha} + j\,\lambda_{L\beta} \tag{50}$$

Based on motor measurements, the real and imaginary parts are calculated by.

$$\lambda_{L\alpha} = \int \left(u_{ab} - R(i_a - i_b)\right)dt \tag{51}$$

$$\lambda_{L\beta} = \int \left(\frac{1}{\sqrt{3}}(u_{ab} + 2u_{bc}) - \sqrt{3}R(i_a + i_b)\right) dt \tag{52}$$

The resulting angular position θ_λ is then employed in the control scheme, incorporating both speed and current loops. Motor currents are compared with reference currents in the current loop, and the error signals are utilized for inverter control.

The control scheme involves positioning the vector in the α-β plane, and the current references for the three phases are calculated accordingly.

$$\begin{bmatrix} i_a^* \\ i_b^* \\ i_c^* \end{bmatrix} = \begin{bmatrix} -sin\,(\theta_s) & cos\,(\theta_s) \\ -sin\,(\theta_s - 2\pi/3) & cos\,(\theta_s - 2\pi/3) \\ -sin\,(\theta_s + 2\pi/3) & cos\,(\theta_s + 2\pi/3) \end{bmatrix} \times \begin{bmatrix} i_s^* \\ 0 \end{bmatrix} \tag{53}$$

where $\bar{\imath}_s^*$ is the output signal from the speed loop PI and θ_s defined as:

$$\bar{\imath}_s^* = i_s^*\, ang(\theta_s + 90°) \tag{54}$$

$$\theta_s = \theta_{\lambda_L} - 30° \tag{55}$$

However, it's noteworthy that positioning $\bar{\imath}_s$ at 90° to $\lambda_{L\beta}$ does not yield the maximum torque on current, as shown in Fig. 9. This limitation arises because the current vector is not aligned with the q-axis. Consequently, the position of the d-q axes or the vector $\bar{\lambda}_{mg}$ remains unknown with this method. As a result, a slightly lower torque is obtained due to the small phase shift between the linked flux caused by the permanent magnet and the total stator flux.

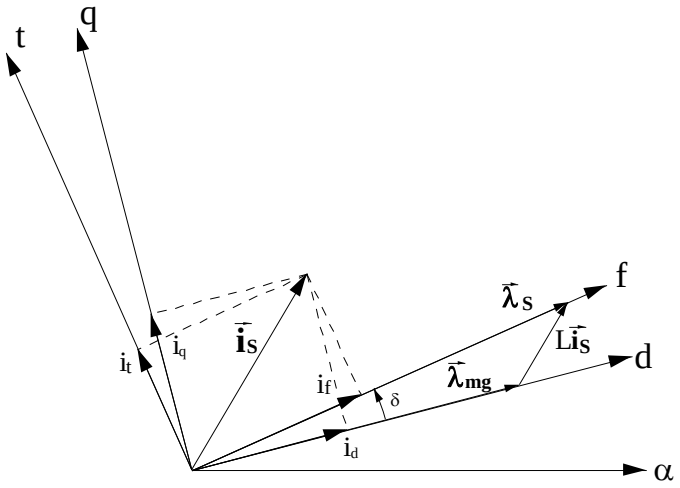

Fig. 9. Phase shift between linked fluxes

$$\tau = \lambda_{ds} i_{qs} - \lambda_{qs} i_{qs} = Im\left(\bar{\lambda}_s \bar{\imath}_s^*\right) = Im\left(|\bar{\lambda}_s| e^{j\theta_s} |i_s| e^{-j\theta_i}\right) \tag{56}$$

$$\tau = |\lambda_s||i_s| sin\,(\theta_s - \theta_i) \tag{57}$$

Moreover, considerations must be made regarding the amplification of high-frequency noise via a derivative, particularly in obtaining the signal proportional to speed θ_{λ_L}. Implementing a low-pass filter becomes imperative to mitigate this effect, as indicated by Equations (58) and (59).

$$F(Z) = \frac{\omega_f}{\omega} = \frac{aT(Z+1)}{(2+aT)Z-(2-aT)} \tag{58}$$

$$\omega_f^n = \left(\frac{2-aT}{2+aT}\right)\omega_f^{n+1} + \left(\frac{aT}{2+aT}\right)(\omega^n + \omega^{n+1}) \tag{59}$$

It is crucial to consider the offset produced by the integrators to ensure accurate results, Integrators are vital for calculating the real and imaginary components of the linked flux, but they introduce errors in estimating the angular position of the spatial vector $\bar{\lambda}_L$. Ideally, this vector should describe a circumference centered at the origin in the α–β plane, but due to the offset, its center is translated by the quantities DR+jDI. This translation affects the flux components $\lambda_{L\alpha}$ and $\lambda_{L\beta}$, causing misestimation of the position of $\bar{\lambda}_L$. This error impacts the calculation of the angle and consequently the speed. Control schematic of sensorless brushless motor shown in Fig. 10.

$$\omega_{\lambda L} = \frac{d\theta'_{\lambda L}}{dt} = \frac{d}{dt}\left[\tan^{-1}\left(\frac{1+DI}{R+DR}\right)\right] \tag{60}$$

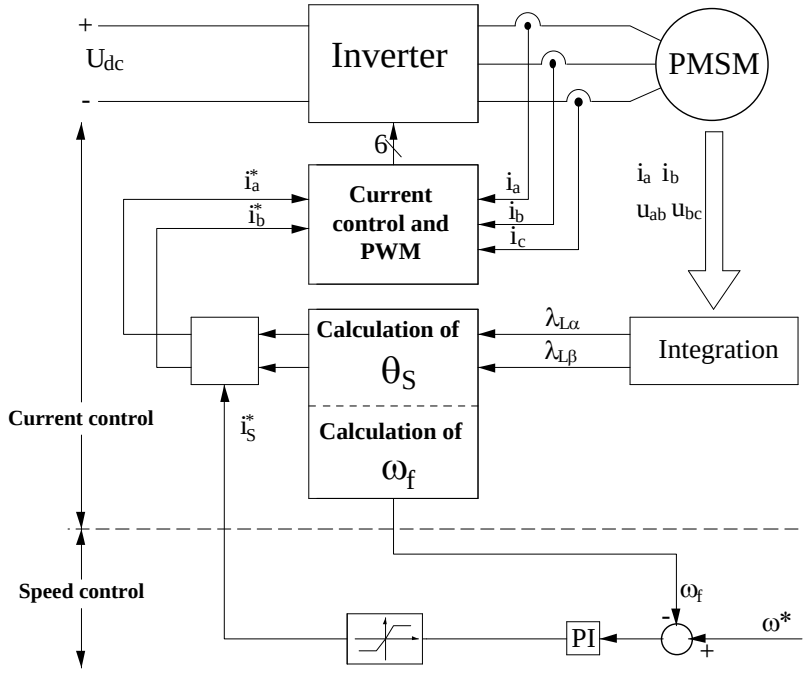

Fig. 10. Control Schematic of Sensorless brushless motor

To mitigate this difference and bring the vector back to the origin, an indispensable compensation procedure must be implemented. This procedure determines specific points (P, Q, T, and S) to calculate the maximum and minimum of the real and imaginary components of the translation vector, allowing the correction of the offset. The off-set vector diagram shown in Fig. 11.

$$DR + jDI = \frac{\lambda'_{L\alpha(max)} + \lambda'_{L\alpha(min)}}{2} + j\frac{\lambda'_{L\beta(max)} + \lambda'_{L\beta(min)}}{2} \tag{61}$$

This correction facilitates obtaining the correct angle of the vector $\bar{\lambda}_L$.

$$\theta_{\lambda L} = \tan^{-1}\left(\frac{\lambda'_{L\alpha} - DR}{\lambda'_{L\beta} - DI}\right) \tag{62}$$

This comprehensive control scheme demonstrates the feasibility of sensorless brushless motor control, relying solely on voltage and current measurements, ensuring the synchronization of motor performance with desired speed references.

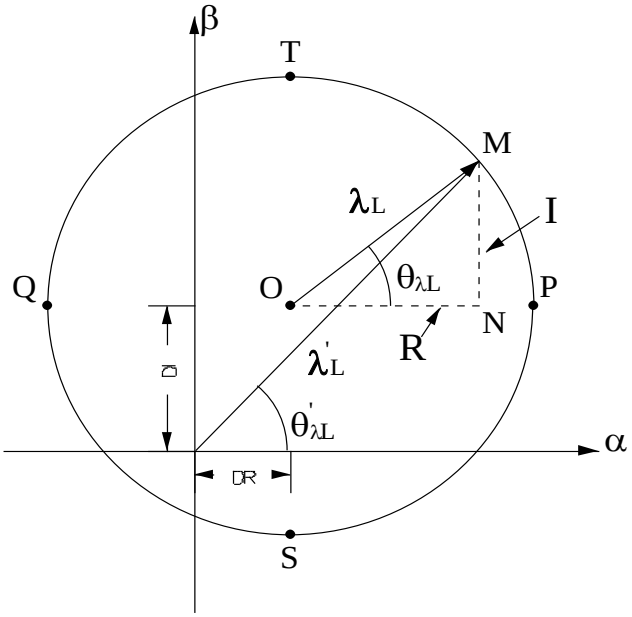

Fig. 11. The off-set vector diagram

4. Results and Discussion

4.1. Results of First Sensorless Topology (Voltage Based)

4.1.1. Low Speed-Unloading Operation

The performance evaluation of Matsui's voltage-based sensorless approach is carried out for three different operating conditions. The first operating condition when the motor rotates at low speed range (10 rad/s) without motor loading. Fig. 12 and Fig. 13 show respectively the actual and estimated speeds and the resultant estimation error. As noticed the average speed error is about 0.1 rad/s. Fig. 14 and Fig. 15 illustrate the developed torque and the its deviation from its reference signal. The torque is appropriately settled at zero Nm. Fig. 16 and Fig. 17 provide in turns the actual and estimated rotor positions and the resultant deviations. It is obvious that the estimation erro exhibits very small value of 0.01 rad. Fig. 18 and Fig. 19, Fig. 20 show respectively the calcualted and reference values of stator current components (i_γ and i_δ). The current deviations are almostly null as illustrated respectively in Fig. 19 and Fig. 21. All of these dynamics approve the validness of the designed vector control for the motor.

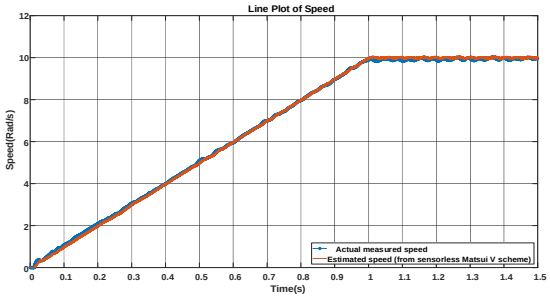

Fig. 12. Actual and estimated speed (low speed-unloaded)

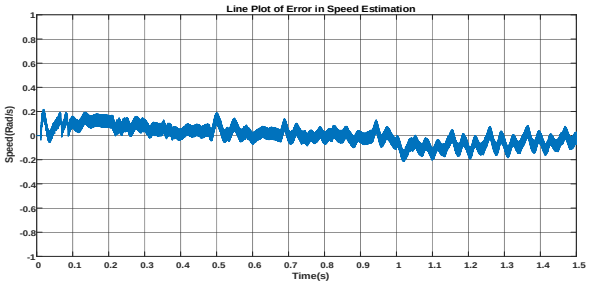

Fig. 13. Speed estimation error (low speed-unloaded)

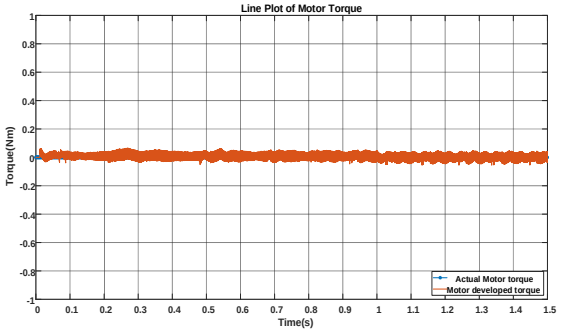

Fig. 14. Estimated and reference torque (low speed-unloaded)

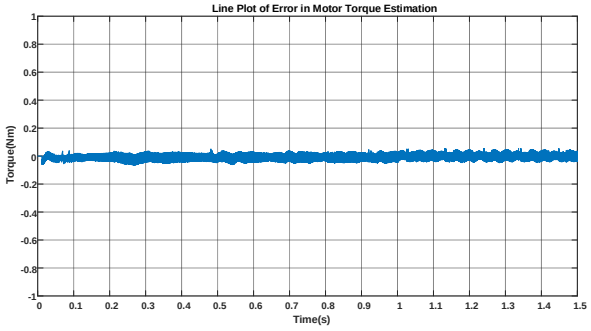

Fig. 15. Torque estimation error (low speed-unloaded)

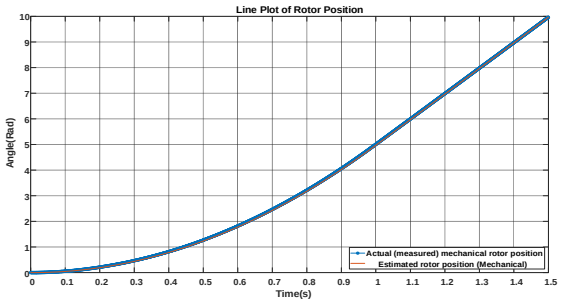

Fig. 16. Actual and estimated rotor position (low speed-unloaded)

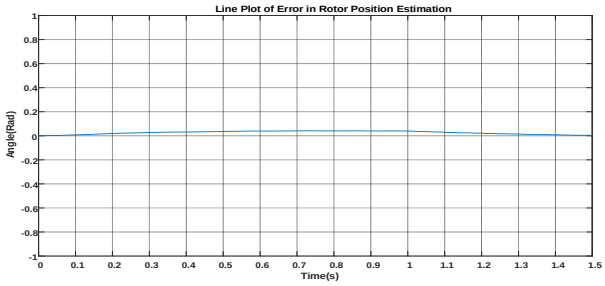

Fig. 17. Rotor position estimation error (low speed-unloaded)

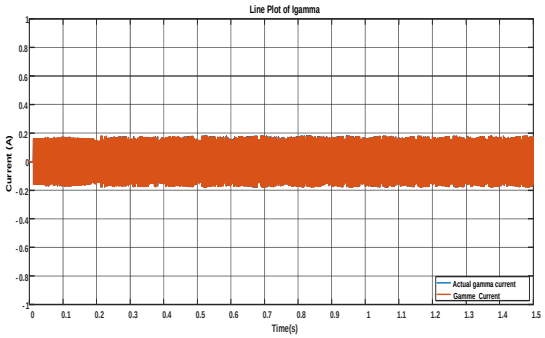

Fig. 18. i_γ current component (low speed-unloaded)

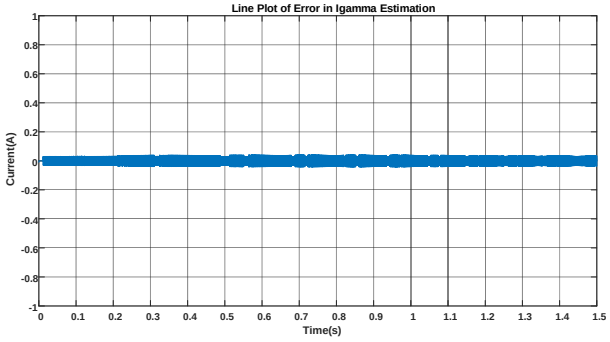

Fig. 19. i_γ current deviation (low speed-unloaded)

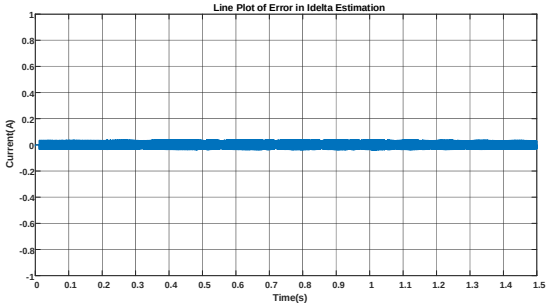

Fig. 20. i_δ current deviation (low speed-unloaded)

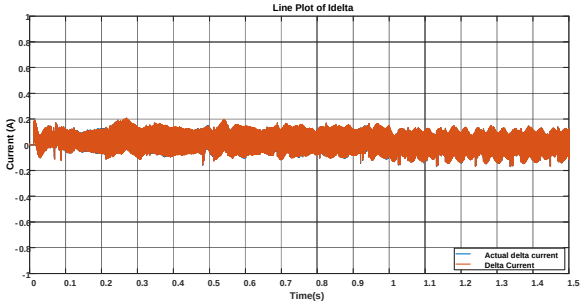

Fig. 21. i_δ current component (low speed-unloaded)

4.1.2. High Speed-Unloading Operation

The second operating condition when the motor rotates at high speed range (100 rad/s) without motor loading. Fig. 22 and Fig. 23 show respectively the actual and estimated speeds and the resultant estimation error. As noticed during acceleration, the average speed error is about 0.65 rad/s. However, when under steady state operation, the speed error is diminished after time t=1.2 sec. Fig. 24 and Fig. 25 illustrate the developed torque and the its deviation from its reference signal. There is a torque deviation of 0.08 Nm during the acceleration interval from starting till time t= 1.2 sec, then the torque deviation is appropriately settled at zero Nm. Fig. 26 and Fig. 27 provide the actual and estimated rotor positions and the resultant errors. During acceleation time, the position error reaches to about 0.2 rad and then settled to zero under steady state operation. Fig. 28 and Fig. 30 show respectively the calcualted and reference values of stator current components (i_γ and i_δ). The current deviations are almostly null as illustrated respectively in Fig. 29 and Fig. 31 which validate the designed vector control scheme.

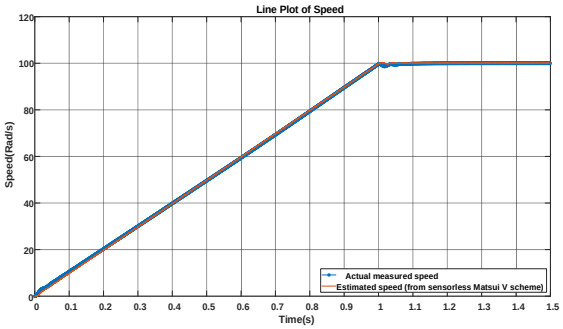

Fig. 22. Actual and estimated speed (high speed-loaded)

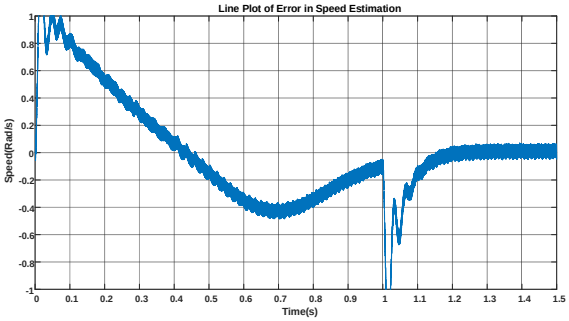

Fig. 23. Speed estimation error (high speed-loaded)

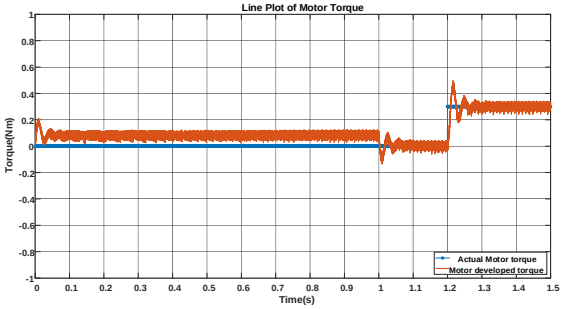

Fig. 24. Estimated and reference torque (high speed-loaded)

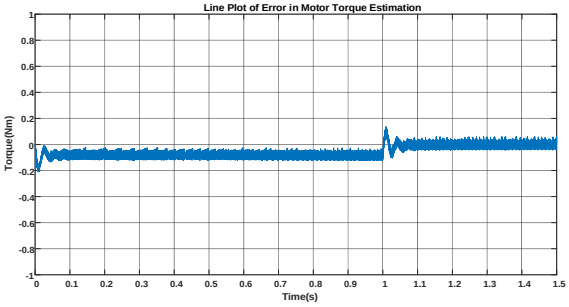

Fig. 25. Torque estimation error (high speed-loaded)

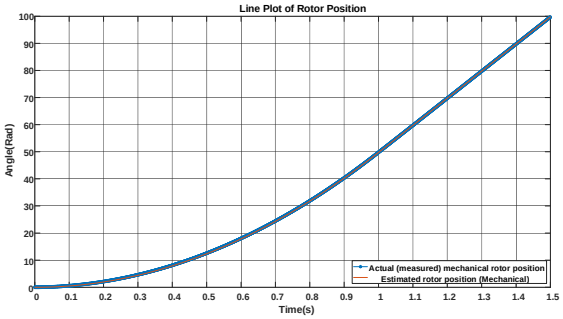

Fig. 26. Actual and estimated rotor position (high speed-loaded)

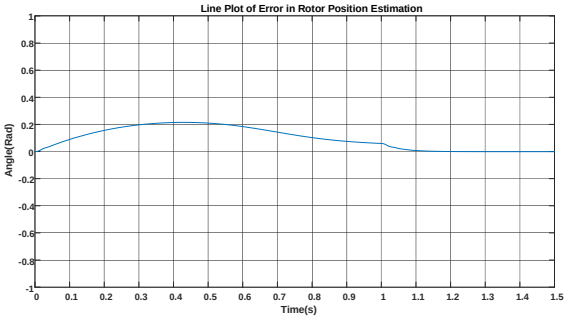

Fig. 27. Rotor position estimation error (high speed-loaded)

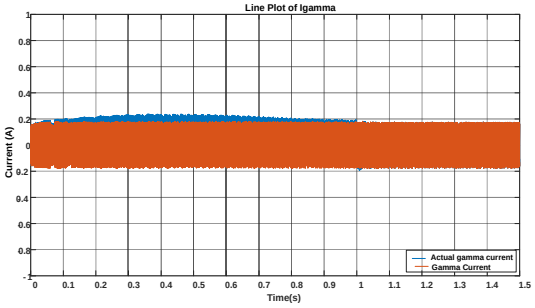

Fig. 28. i_γ current component (high speed-loaded)

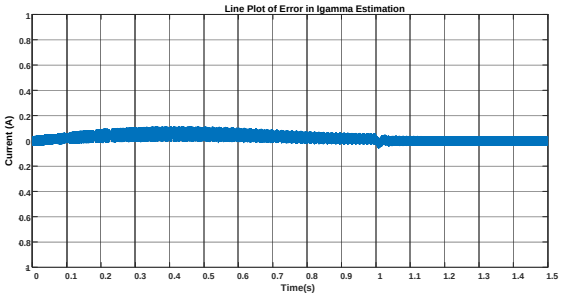

Fig. 29. i_γ current deviation (high speed-loaded)

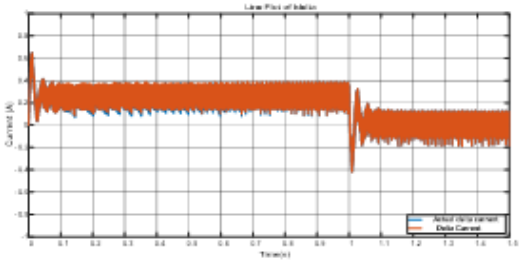

Fig. 30. i_δ current component (high speed-loaded)

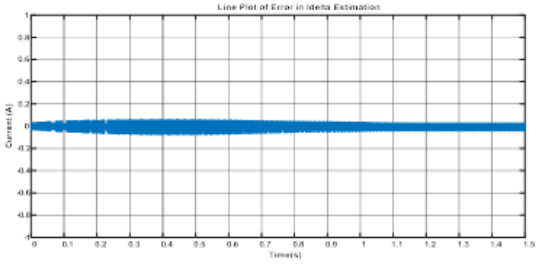

Fig. 31. i_δ current deviation (high speed-loaded)

4.1.3. High Speed-Loading Operation

The third operating condition when the motor rotates at high speed range (100 rad/s) with motor loading of 0.3 Nm at time t=1.2 sec. Fig. 32 and Fig. 33 show accordingly the actual and estimated speeds and the relevant estimation error. As noticed during acceleration, the average speed error is about 0.65 rad/s. Additionally, there is an arburpt speed oscillation at time t=1.2 sec due to applying the load. However, under steady state operation, the speed error is diminished after time t=1.3 sec. Fig. 34 and Fig. 35 illustrate the estimated torque and the its deviation from its reference signal. There is a torque deviation of 0.08 Nm during the acceleration interval from starting till time t= 1.0 sec, then the torque deviation is appropriately settled at zero Nm from t=1.0 to t=1.2 sec; after that an instantaneous toruq deviation is noticed from t=1.2 sec to t=1.3 sec due to applying the load torque. Fig. 36 and Fig. 37 provide the actual and estimated rotor positions and the resultant errors. During acceleation time, the position error reaches to about 0.2 rad and then settled to zero under steady state operation. Fig. 38 and Fig. 40 show respectively the calcualted and reference values of stator current components (i_γ and i_δ). The current i_γ is appropriately settled at zero, mwanhile the current i_δ follows the speed and torque dynamics. The current deviations are almostly null as illustrated respectively in Fig. 39 and Fig. 41.

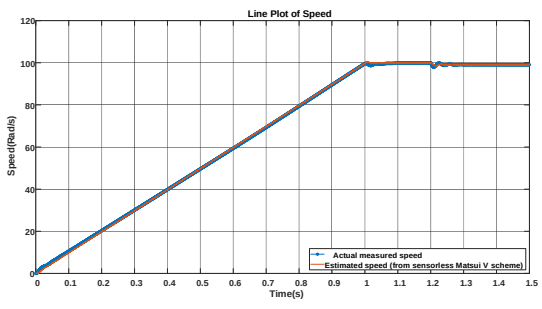

Fig. 32. Actual and estimated speed (high speed-loaded)

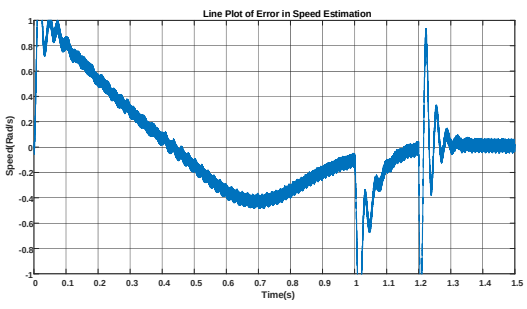

Fig. 33. Speed estimation error (high speed-loaded)

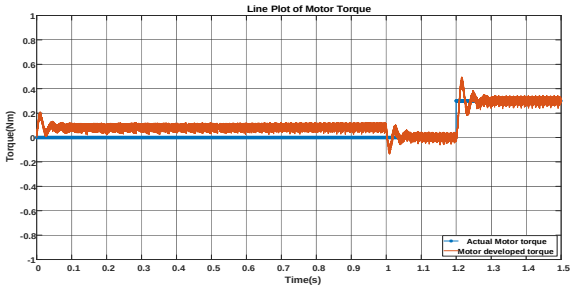

Fig. 34. Estimated and reference torque (high speed-loaded)

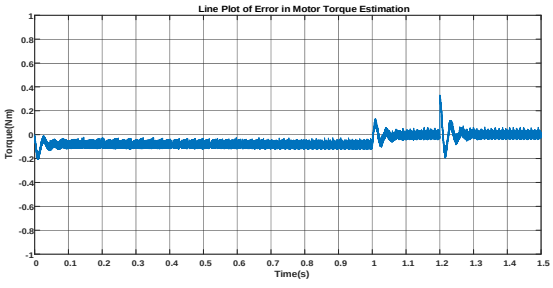

Fig. 35. Torque estimation error (high speed-loaded)

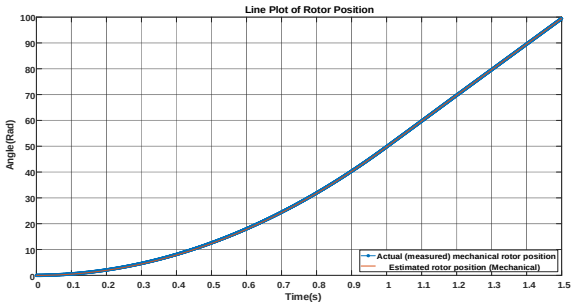

Fig. 36. Actual and estimated rotor position (high speed-loaded)

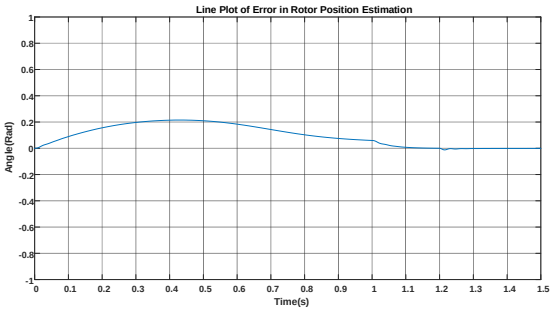

Fig. 37. Rotor position estimation error (high speed-loaded)

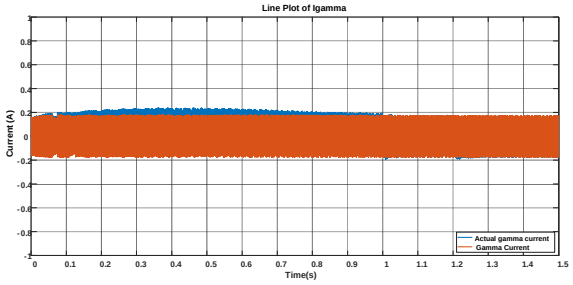

Fig. 38. i_γ current component (high speed-loaded)

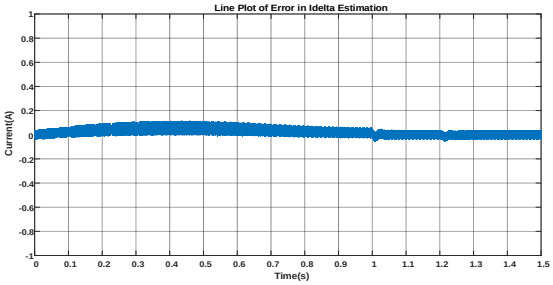

Fig. 39. i_γ current deviation (high speed-loaded)

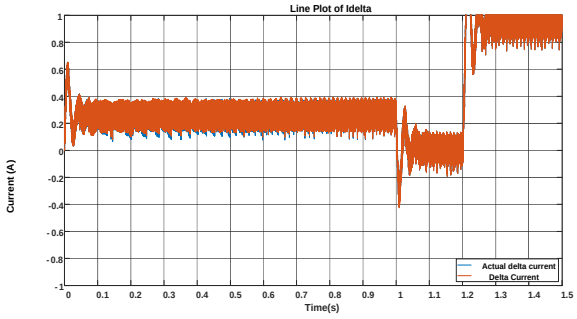

Fig. 40. i_δ current component (high speed-loaded)

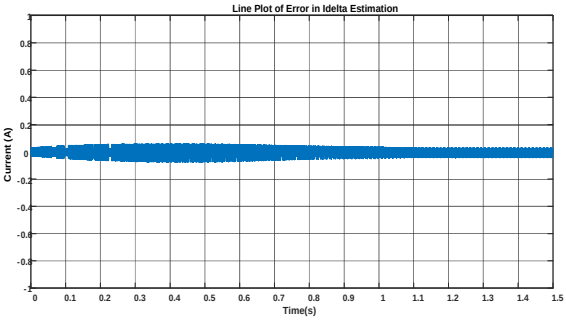

Fig. 41. i_δ current deviation (high speed-loaded)

4.2. Results of Second Sensorless Topology (Current based)

4.2.1. Low Speed-Unloading Operation

The performance evaluation of Matsui's current-based sensorless approach is also perfromed for the same operating conditions as in the Matsui's voltage-based technique. Under low operating speed

condition (10 rad/s) without motor loading, Fig. 42 and Fig. 43 show respectively the actual and estimated speeds and the resultant estimation error. As noticed the speed error is noticeable at starting till time t=0.5 sec, with average value of about 1 rad/s. After that, the speed error is settled to zero. Fig. 44 and Fig. 45 illustrate the developed torque and the its deviation from its reference signal. The torque is appropriately settled at zero Nm. Fig. 46 and Fig. 47 provide in turns the actual and estimated rotor positions and the resultant deviations. It is obvious that the estimation error exhibits an average value of 0.3 rad. Fig. 48 and Fig. 50 show respectively the calcualted and reference values of stator current components (i_γ and i_δ). The current deviations are almostly null as illustrated respectively in Fig. 49 and Fig. 51.

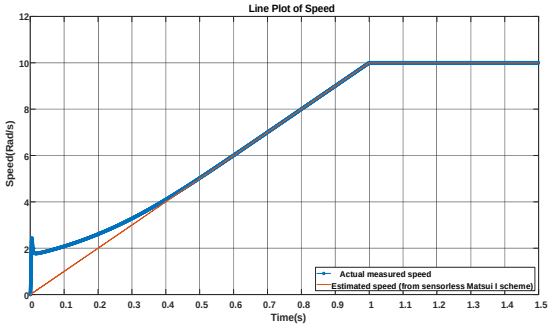

Fig. 42. Actual and estimated speed (low speed-unloaded)

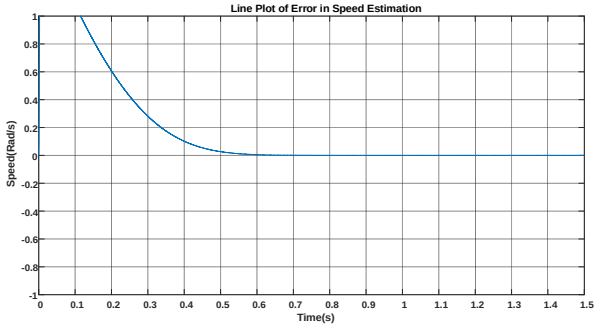

Fig. 43. Speed estimation error (low speed-unloaded)

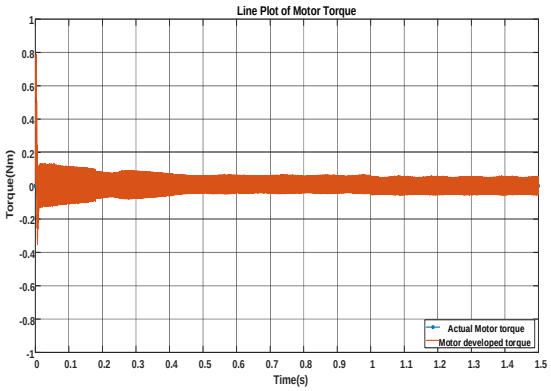

Fig. 44. Estimated and reference torque (low speed-unloaded)

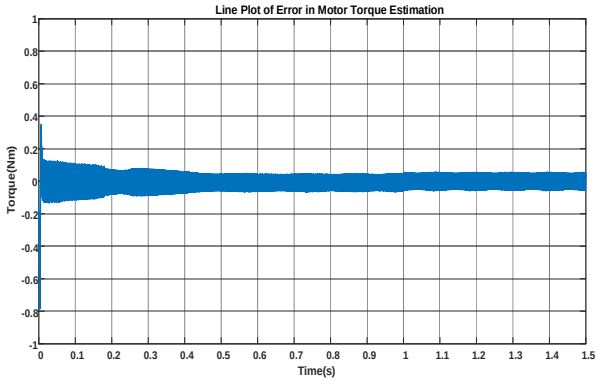

Fig. 45. Torque estimation error (low speed-unloaded)

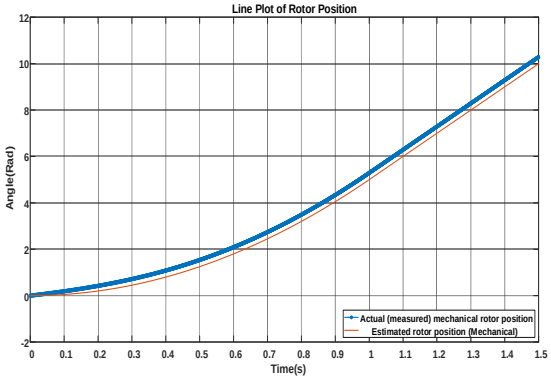

Fig. 46. Actual and estimated rotor position (low speed-unloaded)

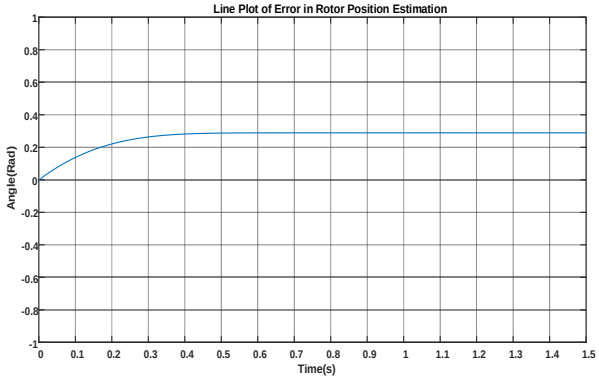

Fig. 47. Rotor position estimation error (low speed-unloaded)

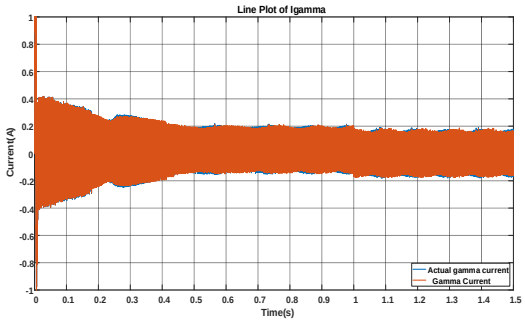

Fig. 48. i_γ current component (low speed-unloaded)

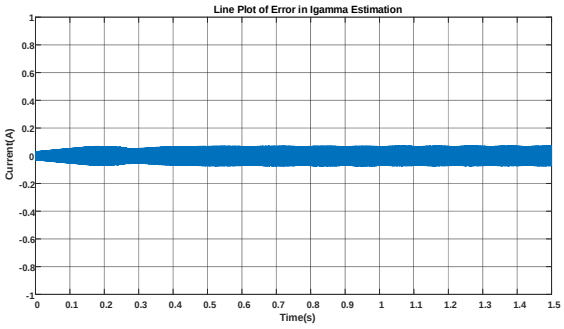

Fig. 49. i_γ current deviation (low speed-unloaded)

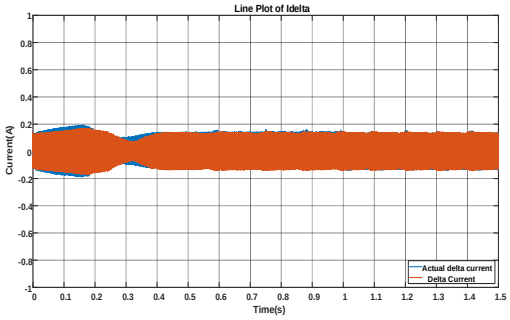

Fig. 50. i_δ current component (low speed-unloaded)

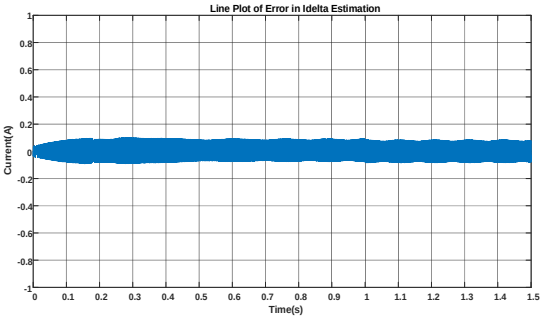

Fig. 51. i_δ current deviation (low speed-unloaded)

4.2.2. High Speed-Unloading Operation

The current-based estiamtion technique is also tested when the motor rotates at high speed range (100 rad/s) without motor loading. Fig. 52 and Fig. 53 show respectively the actual and estimated speeds and the resultant estimation error. As noticed, there a deviation of 1 rad/s from starting to time t=0.18 sec, and then the speed error is settled to zero. Fig. 54 and Fig. 55 illustrate the developed torque and the its deviation from its reference signal. There is a torque deviation of about 0.08 Nm during the acceleration interval from starting till time t= 1.0 sec, then the torque deviation is appropriately settled at zero. Fig. 56 and Fig. 57 illustrate the actual and estimated rotor positions and the resultant errors. The position error exhibits almost constant value of 0.3 rad. Fig. 58 and Fig. 60 show respectively the calcualted and reference values of stator current components (i_γ and i_δ). The current deviation of i_γ exhibits a value of 0.1 A from t=0 to t=1 sec, then it is settled to zero as illustrated in Fig. 59. Meanwhile, the current deviation of i_δ is settled appropriately to zero all the operating period as illustrated in Fig. 61.

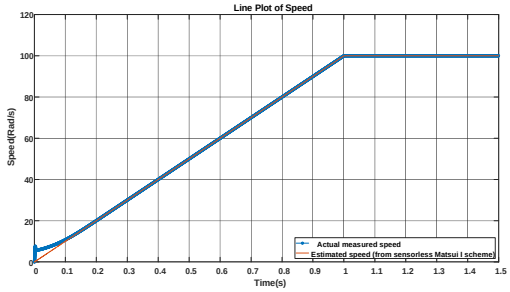

Fig. 52. Actual and estimated speed (high speed-unloaded)

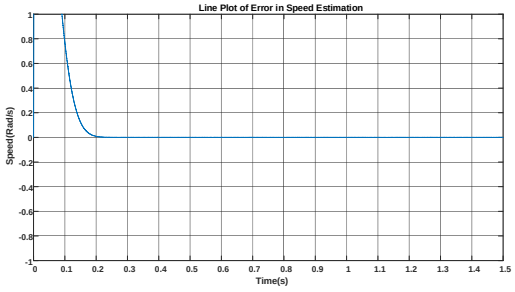

Fig. 53. Speed estimation error (high speed-unloaded)

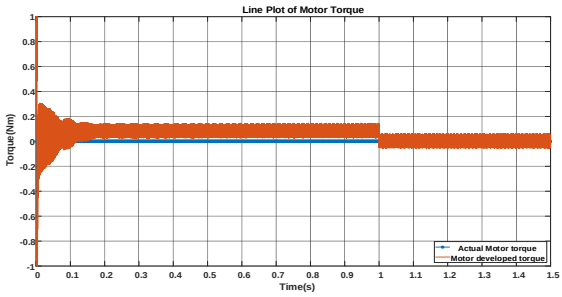

Fig. 54. Estimated and reference torque (high speed-unloaded)

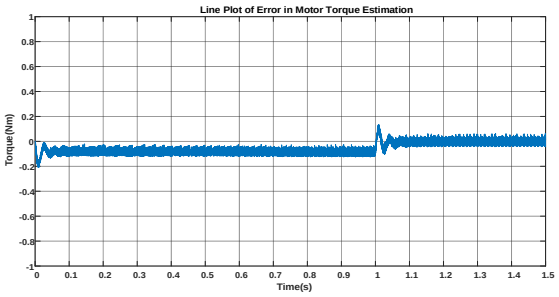

Fig. 55. Torque estimation error (high speed-unloaded)

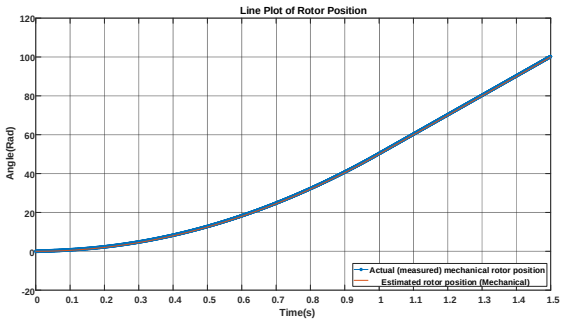

Fig. 56. Actual and estimated rotor position (high speed-unloaded)

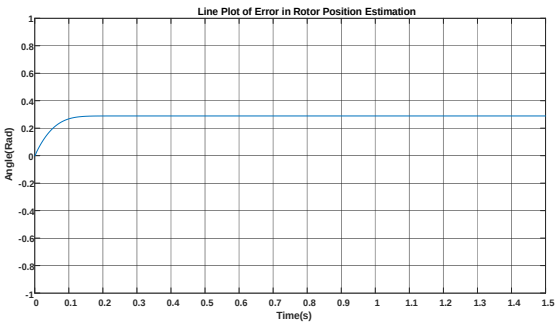

Fig. 57. Rotor position estimation error (high speed-unloaded)

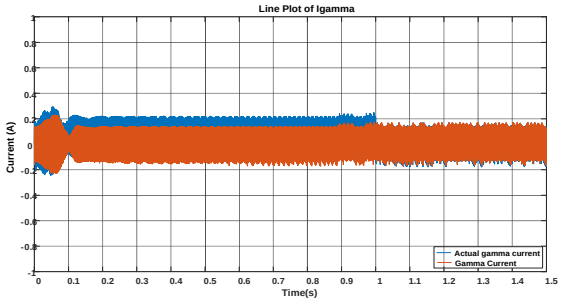

Fig. 58. i_γ current component (high speed-unloaded)

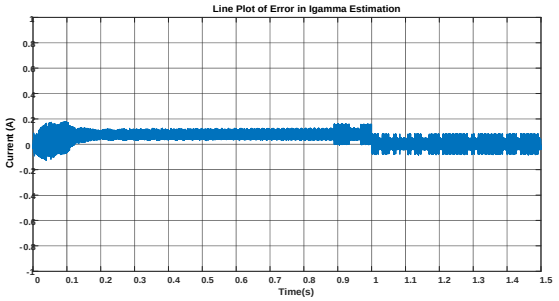

Fig. 59. i_γ current deviation (high speed-unloaded)

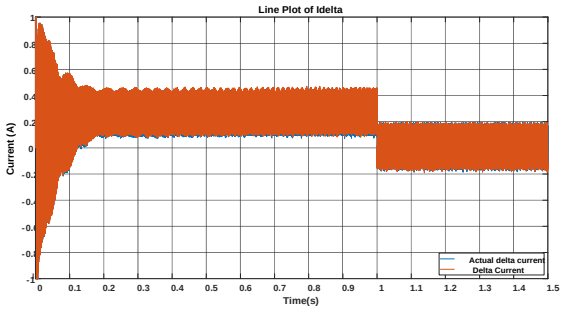

Fig. 60. i_δ current component (high speed-unloaded)

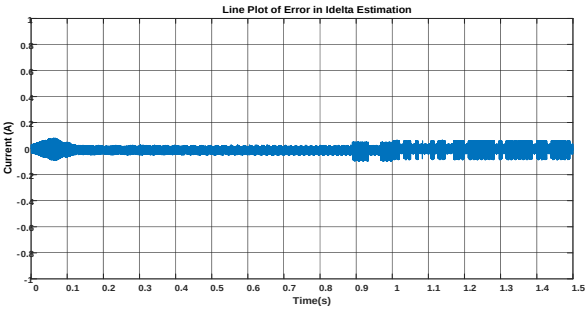

Fig. 61. i_δ current deviation (high speed-unloaded)

4.2.3. High Speed-Loading Operation

The third operating condition for the current-based sensorless approach is when the motor rotates at high speed range (100 rad/s) with motor loading of 0.3 Nm at time t=1.2 sec. Fig. 62 and Fig. 63 illustrate respectively the actual and estimated speeds and the resultant estimation error. As noticed, there is a speed error of 1 rad/s up to time t=0.2 sec, and after that the error is settled at zero. In comparison with the voltage-based technique, there is no observed speed oscillation at time t=1.2 sec due to applying the load. Fig. 64 and Fig. 65 illustrate the estimated torque and the its deviation from its reference signal. There is a torque deviation of 0.08 Nm during the acceleration interval from starting till time t= 1.0 sec, then the torque deviation is appropriately held at zero Nm from t=1.0 to t=1.2 sec; after that an instantaneous torque pulsation is noticed at t=1.2 sec due to applying the load torque. Fig. 66 and Fig. 67 provide the actual and estimated rotor positions and the resultant errors. The position error exhibits about 0.3 rad. Fig. 68 and Fig. 70 show respectively the calcualted and reference values of stator current components (i_γ and i_δ). The current i_γ is appropriately settled at zero, mwanhile the current i_δ follows the speed and torque dynamics.The current i_γ deviation is almostly null as illustrated in Fig. 67, meanwhile there is a deviation in the calculated values of i_δ current with values of 0.1 A from t=0 to t=1 sec aand of 0.3 A from t=1.2 sec to the end as illustrated in Fig. 69 and Fig. 71.

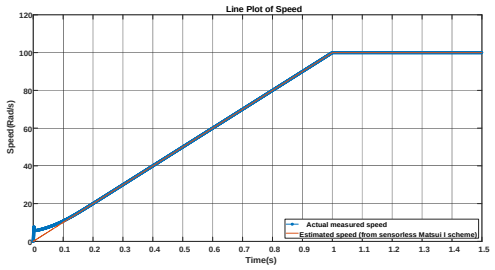

Fig. 62. Actual and estimated speed (high speed-loaded)

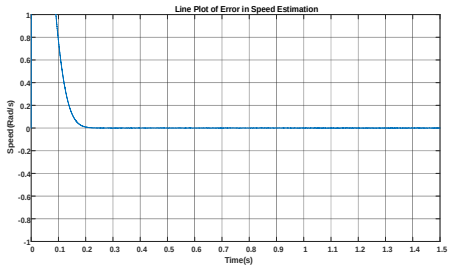

Fig. 63. Speed estimation error (high speed-loaded)

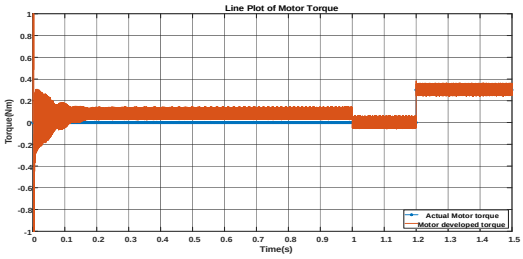

Fig. 64. Estimated and reference torque (high speed-loaded)

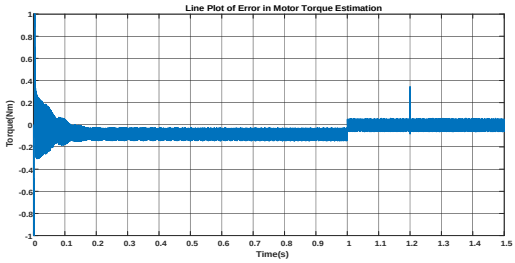

Fig. 65. Torque estimation error (high speed-loaded)

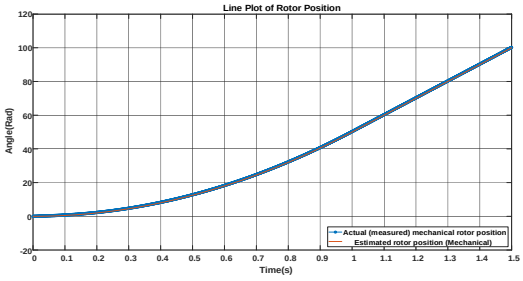

Fig. 66. Actual and estimated rotor position (high speed-loaded)

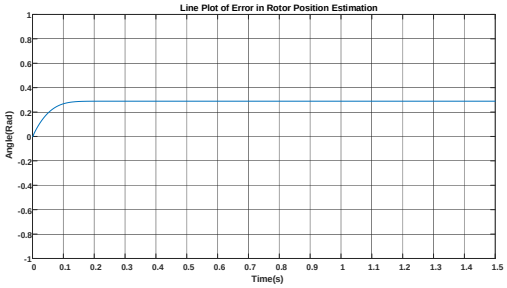

Fig. 67. Rotor position estimation error (high speed-loaded)

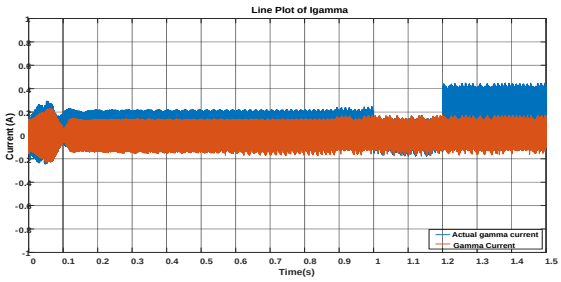

Fig. 68. i_γ current component (high speed-loaded)

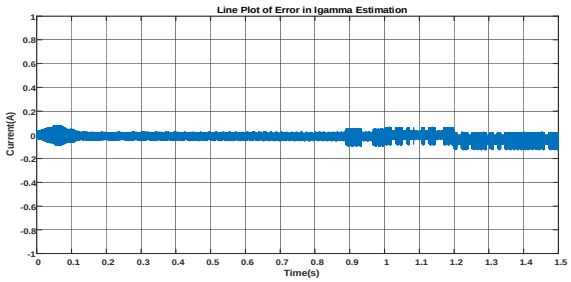

Fig. 69. i_γ current deviation (high speed-loaded)

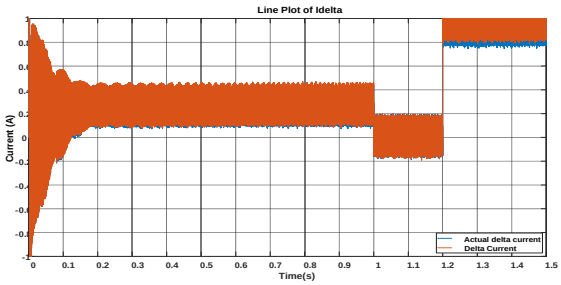

Fig. 70. i_δ current component (high speed-loaded)

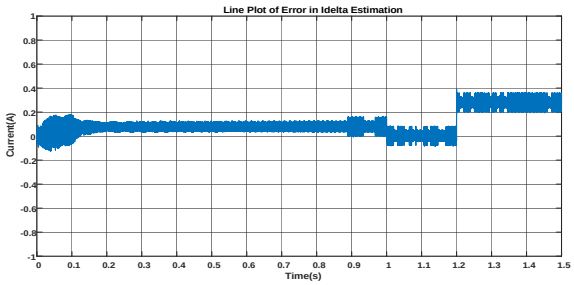

Fig. 71. i_δ current deviation (high speed-loaded)

4.3. Results of Third Sensorless Topology (Flux-Based)

4.3.1. Low Speed-Unloading Operation

The performance evaluation of Slemon's flux-based sensorless approach is also perfromed for the same operating conditions as in the previous two techniques. Under low operating speed condition (10 rad/s) without motor loading, Fig. 72 and Fig. 73 show respectively the actual and estimated speeds and the resultant estimation error. As noticed the speed error is noticeable at starting till time t=1.2 sec, with average value of about 0.8 rad/s. After that, the speed error is settled to zero. Fig. 74 and Fig. 75 illustrate the developed torque and its deviation from its reference signal. The torque is appropriately settled at zero Nm.

Fig. 76 and Fig. 77 provide in turns the actual and estimated rotor positions and the resultant deviations. It is obvious that the estimation error exhibits an average value of 0.1 rad. Fig. 78 and Fig. 79 show respectively the calcualted and reference values of stator current components (i_γ and i_δ). The current deviations are almostly null as illustrated respectively in Fig. 79 and Fig. 81.

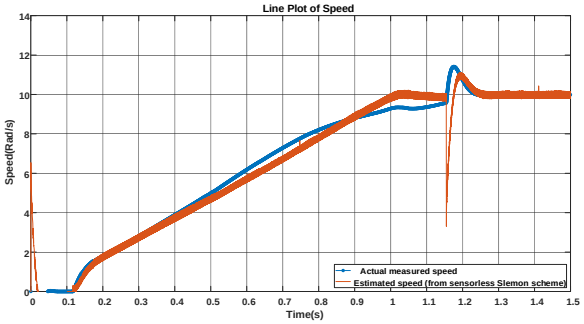

Fig. 72. Actual and estimated speed (low speed-unloaded)

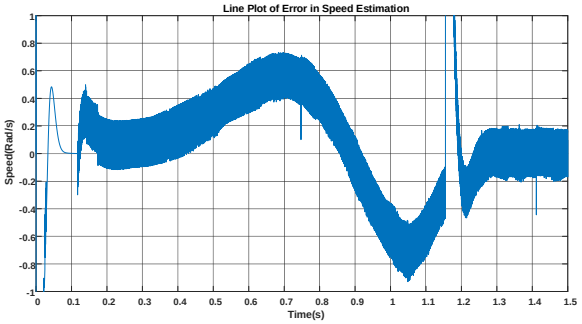

Fig. 73. Speed estimation error (low speed-unloaded)

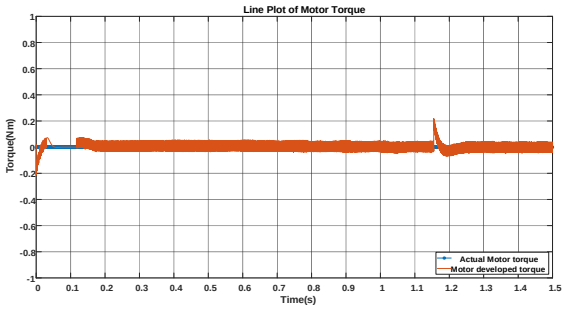

Fig. 74. Estimated and reference torque (low speed-unloaded)

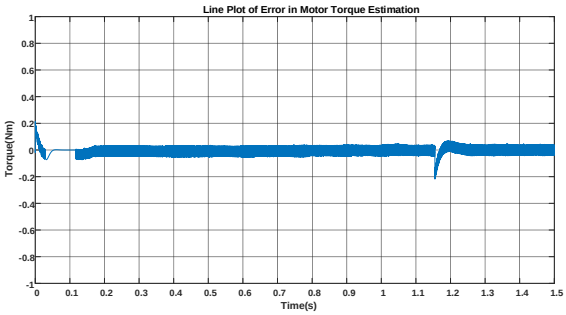

Fig. 75. Torque estimation error (low speed-unloaded)

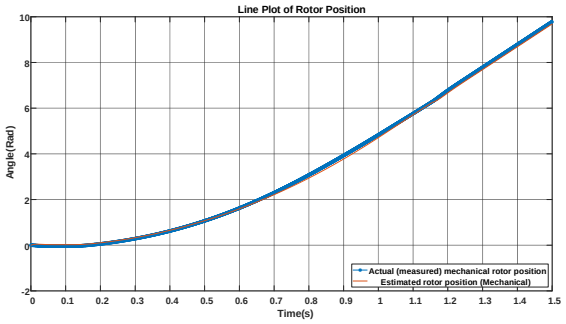

Fig. 76. Actual and estimated rotor position (low speed-unloaded)

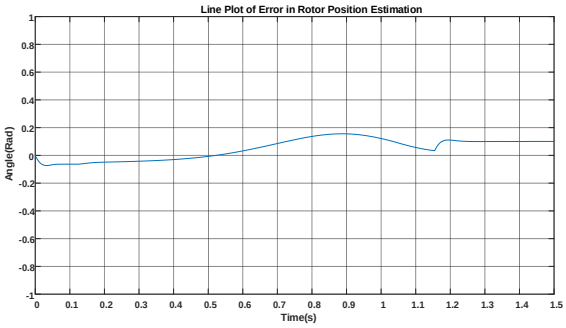

Fig. 77. Rotor position estimation error (low speed-unloaded)

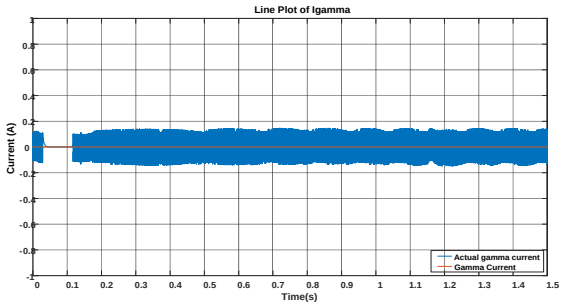

Fig. 78. i_γ current component (low speed-unloaded)

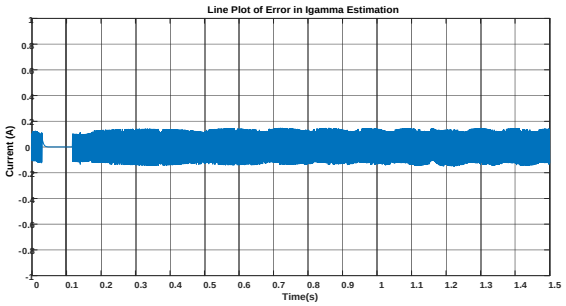

Fig. 79. i_γ current deviation (low speed-unloaded)

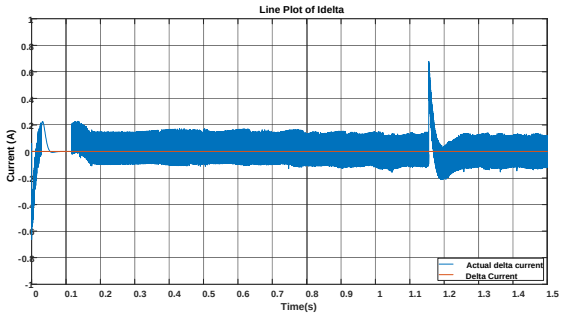

Fig. 80. i_δ current component (low speed-unloaded)

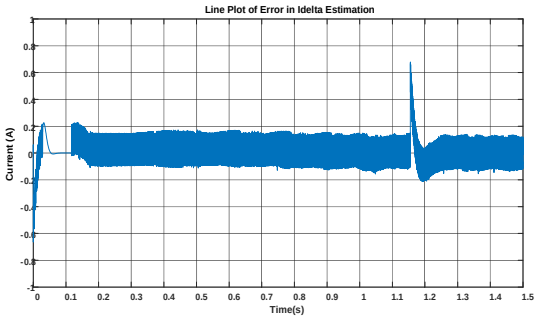

Fig. 81. i_δ current deviation (low speed-unloaded)

4.3.2. High Speed-Unloading Operation

The flux-based estiamtion technique is also tested when the motor rotates at high speed range (100 rad/s) without motor loading. Fig. 82 and Fig. 83 illustrate respectively the actual and estimated speeds and the resultant estimation error. As noticed, there a deviation of 1 rad/s from starting to time t=0.28 sec, and then the speed error is reversed to be -1 rad/s, then from t=0.4 to t=1 sec the error is again 1 rad/s. Finally the speed error is settled to zero from t=1.1 sec. Fig. 84 and Fig. 85 illustrate the developed torque and its deviation from its reference signal. There is a torque deviation of about 0.1 Nm during the acceleration interval from starting till time t= 1.0 sec, then the torque deviation is appropriately settled at zero. Fig. 86 and Fig. 87 illustrate the actual and estimated rotor positions and the resultant errors. The position error exhibits almost average value of 0.5 rad. Fig. 88 and Fig. 90 show respectively the calcualted and reference values of stator current components (i_γ and i_δ). The current deviation of i_γ exhibits an average value of 0.2 A from t=0.4 to t=1 sec, then it is settled to zero as illustrated in Fig. 89. Meanwhile, the current deviation of i_δ exhibits an error of 0.2 A from t=0 to t=1 sec, and then settles as in Fig. 91.

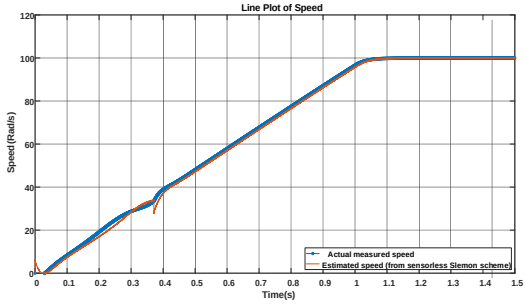

Fig. 82. Actual and estimated speed (high speed-unloaded)

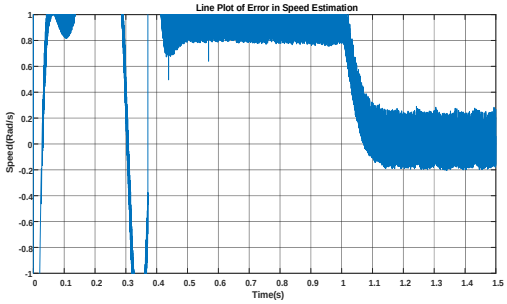

Fig. 83. Speed estimation error (high speed-unloaded)

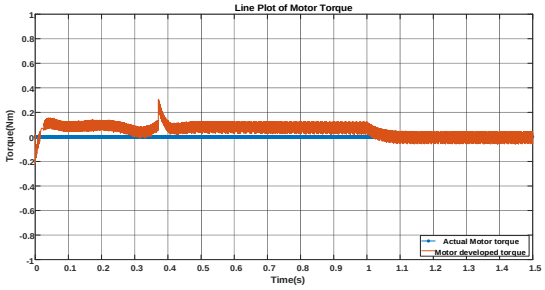

Fig. 84. Estimated and reference torque (high speed-unloaded)

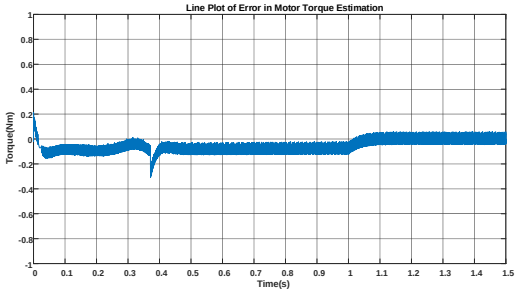

Fig. 85. Torque estimation error (high speed-unloaded)

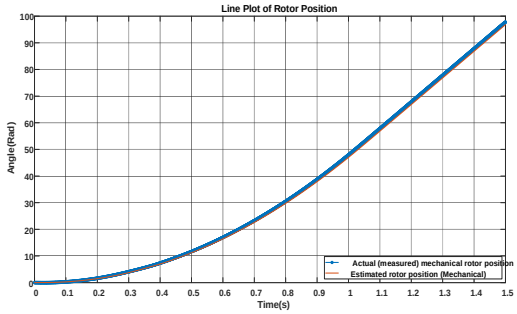

Fig. 86. Actual and estimated rotor position (high speed-unloaded)

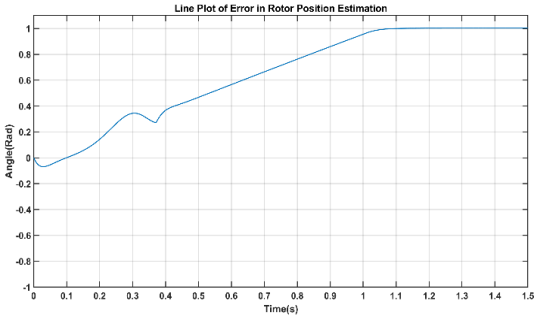

Fig. 87. Rotor position estimation error (high speed-unloaded)

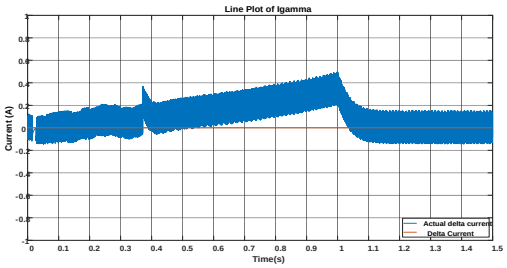

Fig. 88. i_γ current component (high speed-unloaded)

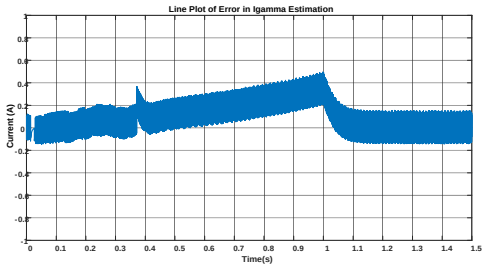

Fig. 89. i_γ current deviation (high speed-unloaded)

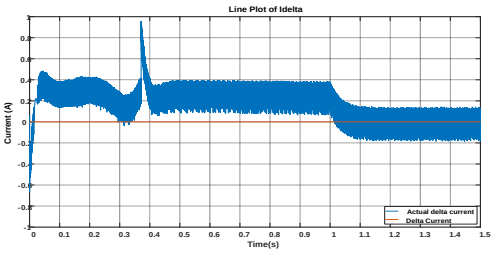

Fig. 90. i_δ current component (high speed-unloaded)

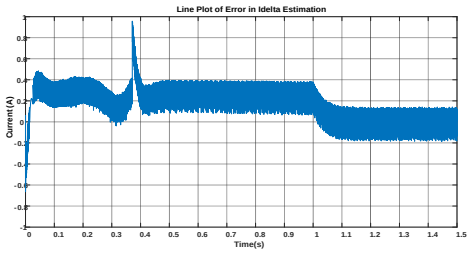

Fig. 91. i_δ current deviation (high speed-unloaded)

4.3.3. High Speed-Loading Operation

The third operating condition for the flux-based sensorless approach is when the motor rotates at high-speed range (100 rad/s) with motor loading of 0.3 Nm at time t=1.2 sec. Fig. 92 and Fig. 93 illustrate respectively the actual and estimated speeds and the resultant estimation error. As noticed, there is a speed error of 1 rad/s up to time t=1 sec, and after that the error is settled at zero. In addition, there is a remarkable speed reduction due to loading in contrast to the other two sensorless techniques. Similar to the voltage-based technique, there is observed speed undershoot at time t=1.2 sec due to applying the load. Fig. 94 and Fig. 95 illustrate the estimated torque and the its deviation from its reference signal. There is a torque deviation of 0.08 Nm during the acceleration interval from starting till time t= 1.0 sec, then the torque deviation is appropriately held at zero Nm from t=1.0 to t=1.2 sec; after that an instantaneous torque pulsation is noticed at t=1.2 sec due to applying the load torque. Fig. 96 and Fig. 97 provide the actual and estimated rotor positions and the resultant errors. The position error exhibits about 0.5 rad. Fig. 98 and Fig. 100 show respectively the calcualted and reference values of stator current components (i_γ and i_δ). The current i_γ exhibits different deviations as 0.2 A from t=0.4 to t=1 sec and 1 A from t=1.2 sec to the end as illustrated in Fig. 99. Meanwhile, the current i_δ follows the speed and torque dynamics. Alternatively, the current i_δ exhibits errors values of 0.2 A from t=0 to t=1 sec and of 1 A from t=1.2 sec to the end as illustrated in Fig. 101.

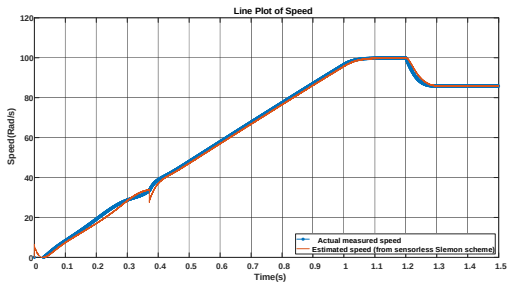

Fig. 92. Actual and estimated speed (high speed-loaded)

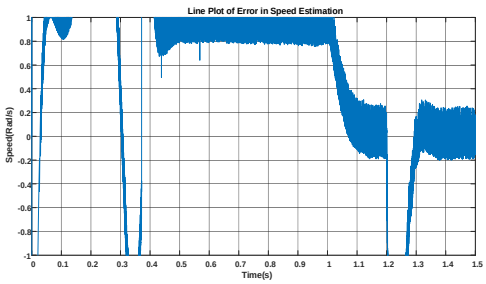

Fig. 93. Speed estimation error (high speed-loaded)

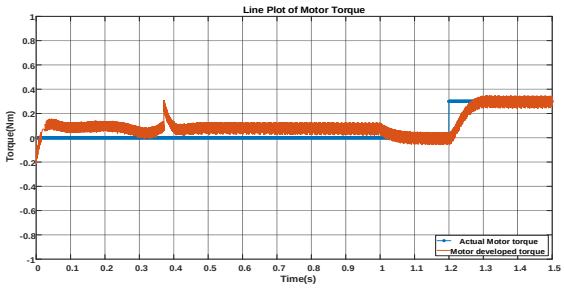

Fig. 94. Estimated and reference torque (high speed-loaded)

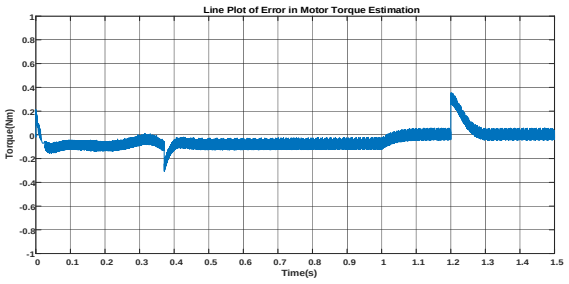

Fig. 95. Torque estimation error (high speed-loaded)

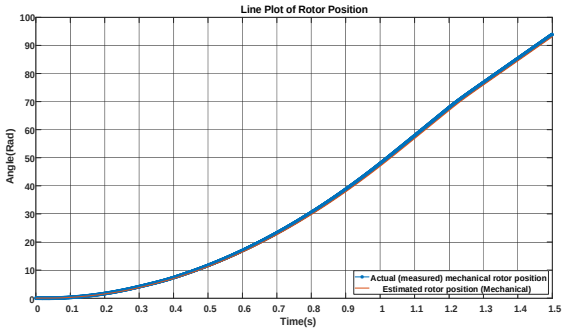

Fig. 96. Actual and estimated rotor position (high speed-loaded)

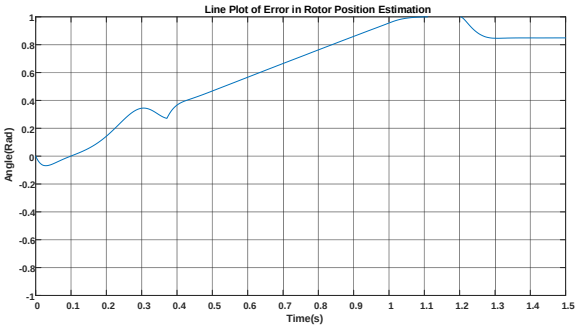

Fig. 97. Rotor position estimation error (high speed-loaded)

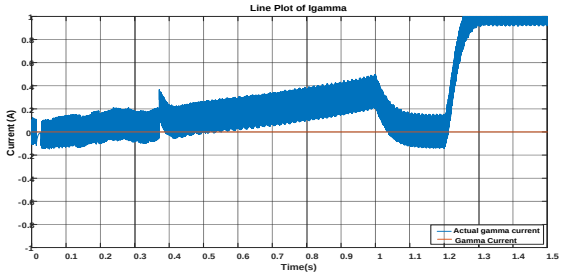

Fig. 98. i_γ current component (high speed-loaded)

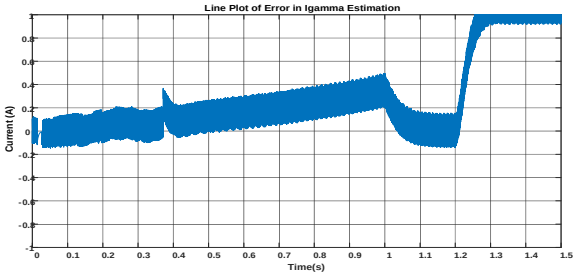

Fig. 99. i_γ current deviation (high speed-loaded)

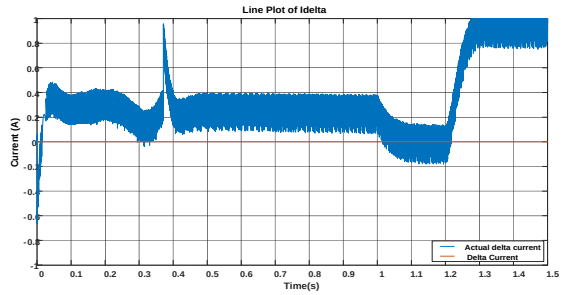

Fig. 100. i_δ current component (high speed-loaded)

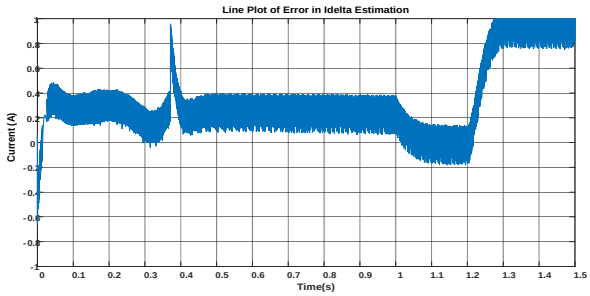

Fig. 101. i_δ current deviation (high speed-loaded)

4.4. Comparative Results

In order to facilitate a comprehensive assessment of the three sensorless motor control methods, Matsui's Voltage-Based, Matsui's Current-Based, and Slemon's Approach, a comparative analysis

has been conducted. Table I below presents a detailed overview of their performance characteristics, highlighting key aspects such as speed estimation errors and rotor position estimation errors.

After evaluating the performance of the three adopted approaches, the choice of the best method depends on the specific priorities of the motor control application. If dynamic behavior and accurate speed estimation at both high and low speeds are paramount, Matsui's Voltage-Based approach may be preferred. On the other hand, if stability in speed estimation and resilience in rotor position estimation are crucial, Matsui's Current-Based approach stands out. Slemon's approach demonstrates a notable trade-off, excelling in low-speed accuracy while maintaining acceptable accuracy at higher speeds.

Table 1. Comparative description of three adopted sensorless schemes

Aspect	Matsui's Voltage-Based	Matsui's Current-Based	Slemon's Approach
Methodology	Utilizes voltage-based algorithms for speed and position estimation. Involves complex mathematical models and real-time calculations.	Relies on current-based algorithms, integrating real-time current measurements for estimation.	Incorporates advanced algorithms for both speed and position estimation, utilizing back electromotive force (EMF) and current sensing. Employs observer and filters for enhanced accuracy.
Speed Estimation	Pronounced error during start-up and high speeds; diminishes with consistent operation, low oscillation at low speeds	Notable error at start-up and very low speeds; diminishes over time, approaching zero	High error during speed ramping, decreases and stabilizes at desired speed, slight oscillation
Rotor Position Estimation	Peak error during speed ramping, gradually reducing to small steady-state error	Steady-state value, showing resilience to changes in speed	Significant error at high speeds, gradually diminishing to low values at slower speeds
Method Characteristics	Sensitivity to speed changes, dynamic behavior	More stability in speed estimation, resilient rotor position estimation	Distinct behavior with high-speed accuracy trade-off at lower speeds

5. Conclusion

In conclusion, this study has explored and compared three sensorless motor control methods—Matsui's Voltage-Based, Matsui's Current-Based, and Slemon's Approach (flux-based). The detailed analysis of their performance characteristics, including speed and rotor position estimation errors, provides valuable insights for researchers and engineers in selecting the most suitable method for their specific applications. Each method exhibits distinct strengths and weaknesses, catering to different operational priorities. Matsui's Voltage-Based approach excels in dynamic speed behavior, while Matsui's Current-Based approach prioritizes stability in speed estimation. Slemon's approach offers to some extent an acceptable high-speed dynamics and suitable performance at lower speeds. However the Slemon's performance comes after the first two sensorless techniques. Statistically, it is found that the voltage-based estimation technique gives respectively lower speed and position estimation errors with percentages of 35% and 10% lower than their values under the current-based estimation technique, and with percentages of 35% and 30% lower than their values under the third adopted scheme. The choice among these methods ultimately depends on the specific requirements of the motor control system, ensuring a tailored and effective solution for diverse applications. As technology advances and application demands evolve, ongoing research in sensorless motor control continues to contribute to the refinement and development of innovative techniques in this critical field.

Author Contribution: All authors contributed equally to the main contributor to this paper. All authors read and approved the final paper.

Funding: This research received no external funding.

Conflicts of Interest: The authors declare no conflict of interest.

Appendix

Table 2. Parameters of Brushless AC Motor

Parameter	Value
R	0.75 Ω
L	$3.05*10^{-3}$ H
λ_{mg}	0.215 Wb
J	$8.26*10^{-4}$ Nm/(rad/s^2)
B	0 Nm/(rad/s)
U_{dc}	160 V
Pole pairs	1

References

[1] Y. Nadjai, H. Ahmed, N. Takorabet, P. Haghgooei, "Maximum Torque per Ampere Control of Permanent Magnet Assisted Synchronous Reluctance Motor: An Experimental Study," *International Journal of Robotics and Control Systems*, vol. 1, no. 4, pp. 416-427, 2021, https://doi.org/10.31763/ijrcs.v1i4.451.

[2] J. Dilys, V. Stankevic, "A Simple Method for Stator Inductance and Resistance Estimation for PMSM at Standstill," *International Journal of Robotics and Control Systems*, vol. 2, no. 3, pp. 477-491, 2022, https://doi.org/10.31763/ijrcs.v2i3.741.

[3] O. Tola, E. Umoh, E. Yahaya, "Pulse Width Modulation Analysis of Five-Level Inverter- Fed Permanent Magnet Synchronous Motors for Electric Vehicle Applications," *International Journal of Robotics and Control Systems*, vol. 1, no. 4, pp. 477-487, 2021, https://doi.org/10.31763/ijrcs.v1i4.483.

[4] M. A. Mossa, O. Gam, N. Bianchi and N. V. Quynh, "Enhanced Control and Power Management for a Renewable Energy-Based Water Pumping System," *IEEE Access*, vol. 10, pp. 36028-36056, 2022, https://doi.org/10.1109/ACCESS.2022.3163530.

[5] B. Bourouba, S. Ladaci, R. Illoul, "Robust Fuzzy Adaptive Control with MRAC Configuration for a Class of Fractional Order Uncertain Linear Systems," *International Journal of Robotics and Control Systems*, vol. 1, no. 3, pp. 326-337, 2021, https://doi.org/10.31763/ijrcs.v1i3.426.

[6] R. Mohamed, M. A. Mossa, A. El-Gaafary, "Performance Enhancement of a Variable Speed Permanent Magnet Synchronous Generator Used for Renewable Energy Application," *International Journal of Robotics and Control Systems*, vol. 3, no. 3, pp. 530-560, 2023, https://doi.org/10.31763/ijrcs.v3i3.1031.

[7] M. A. Mossa, O. Gam, and N. Bianchi, "Dynamic performance enhancement of a renewable energysystem for grid connection and stand-alone operation with battery storage," *Energies*, vol. 15, no. 3, p. 1002, 2022, https://doi.org/10.3390/en15031002.

[8] I. Baik, K. Kim and M. Youn, "Robust nonlinear speed control of PM synchronous motor using boundary layer integral sliding mode control technique," *IEEE Transactions on Control Systems Technology*, vol. 8, no. 1, pp. 47-54, 2000, https://doi.org/10.1109/87.817691.

[9] J. Linares-Flores, C. García-Rodríguez, H. Sira-Ramírez and O. D. Ramírez-Cárdenas, "Robust Backstepping Tracking Controller for Low-Speed PMSM Positioning System: Design, Analysis, and Implementation," *IEEE Transactions on Industrial Informatics*, vol. 11, no. 5, pp. 1130-1141, 2015, https://doi.org/10.1109/TII.2015.2471814.

[10] M. A. Mossa and S. Bolognani, "Predictive Power Control for a Linearized Doubly Fed Induction Generator Model," *2019 21st International Middle East Power Systems Conference (MEPCON)*, pp. 250-257, 2019, https://doi.org/10.1109/MEPCON47431.2019.9008085.

[11] S. Wang, "Nonlinear Uncertainty Estimator-Based Robust Control for PMSM Servo Mechanisms With Prescribed Performance," *IEEE Transactions on Transportation Electrification*, vol. 9, no. 2, pp. 2535-2543, 2023, https://doi.org/10.1109/TTE.2022.3212671.

[12] Y. Zhao, H. Yu and S. Wang, "Development of Optimized Cooperative Control Based on Feedback Linearization and Error Port-Controlled Hamiltonian for Permanent Magnet Synchronous Motor," *IEEE Access*, vol. 9, pp. 141036-141047, 2021, https://doi.org/10.1109/ACCESS.2021.3119625.

[13] Z. Xu, T. Zhang, Y. Bao, H. Zhang and C. Gerada, "A Nonlinear Extended State Observer for Rotor Position and Speed Estimation for Sensorless IPMSM Drives," *IEEE Transactions on Power Electronics*, vol. 35, no. 1, pp. 733-743, 2020, https://doi.org/10.1109/TPEL.2019.2914119.

[14] Y. Zhao, W. Qiao and L. Wu, "Improved Rotor Position and Speed Estimators for Sensorless Control of Interior Permanent-Magnet Synchronous Machines," *IEEE Journal of Emerging and Selected Topics in Power Electronics*, vol. 2, no. 3, pp. 627-639, 2014, https://doi.org/10.1109/JESTPE.2014.2298433.

[15] Q. An and L. Sun, "On-line parameter identification for vector controlled PMSM drives using adaptive algorithm," *2008 IEEE Vehicle Power and Propulsion Conference*, pp. 1-6, 2008, https://doi.org/10.1109/VPPC.2008.4677634.

[16] Suryakant, M. Sreejeth and M. Singh, "Sensorless control of PMSM Drive with BEMF based MRAC Algorithm," *2019 International Symposium on Advanced Electrical and Communication Technologies (ISAECT)*, pp. 1-6, 2019, https://doi.org/10.1109/ISAECT47714.2019.9069705.

[17] N. Matsui and M. Shigyo, "Brushless DC motor control without position and speed sensors," *IEEE Transactions on Industry Applications*, vol. 28, no. 1, pp. 120-127, 1992, https://doi.org/10.1109/28.120220.

[18] N. Matsui, "Sensorless PM brushless DC motor drives," *IEEE Transactions on Industrial Electronics*, vol. 43, no. 2, pp. 300-308, 1996, https://doi.org/10.1109/41.491354.

[19] Z. Yin, Y. Zhang, X. Cao, D. Yuan and J. Liu, "Estimated Position Error Suppression Using Novel PLL for IPMSM Sensorless Drives Based on Full-Order SMO," *IEEE Transactions on Power Electronics*, vol. 37, no. 4, pp. 4463-4474, 2022, https://doi.org/10.1109/TPEL.2021.3125024.

[20] T. Liu, Z. Q. Zhu, Z. -Y. Wu, D. Stone and M. Foster, "A Simple Sensorless Position Error Correction Method for Dual Three-Phase Permanent Magnet Synchronous Machines," *IEEE Transactions on Energy Conversion*, vol. 36, no. 2, pp. 895-906, 2021, https://doi.org/10.1109/TEC.2020.3023904.

[21] K. Liu and Z. Q. Zhu, "Position Offset-Based Parameter Estimation for Permanent Magnet Synchronous Machines Under Variable Speed Control," *IEEE Transactions on Power Electronics*, vol. 30, no. 6, pp. 3438-3446, 2015, https://doi.org/10.1109/TPEL.2014.2337011.

[22] G. Wang *et al*., "Enhanced Position Observer Using Second-Order Generalized Integrator for Sensorless Interior Permanent Magnet Synchronous Motor Drives," *IEEE Transactions on Energy Conversion*, vol. 29, no. 2, pp. 486-495, 2014, https://doi.org/10.1109/TEC.2014.2311098.

[23] R. Lagerquist, I. Boldea and T. J. E. Miller, "Sensorless-control of the synchronous reluctance motor," *IEEE Transactions on Industry Applications*, vol. 30, no. 3, pp. 673-682, 1994, https://doi.org/10.1109/28.293716.

[24] H. Watanabe, S. Miyazaki and T. Fujii, "Improved variable speed sensorless servo system by disturbance observer," *[Proceedings] IECON '90: 16th Annual Conference of IEEE Industrial Electronics Society*, vol. 1, pp. 40-45, 1990, https://doi.org/10.1109/IECON.1990.149107.

[25] S. B. Ozturk and H. A. Toliyat, "Direct Torque and Indirect Flux Control of Brushless DC Motor," *IEEE/ASME Transactions on Mechatronics*, vol. 16, no. 2, pp. 351-360, 2011, https://doi.org/10.1109/TMECH.2010.2043742.

[26] B. Saha and B. Singh, "A Position Sensorless Brushless DC Motor Drive with Inherent Torque Control for EV Application," *2022 IEEE International Conference on Power Electronics, Drives and Energy Systems (PEDES)*, pp. 1-6, 2022, https://doi.org/10.1109/PEDES56012.2022.10080095.

[27] Joohn-Sheok Kim and S. -K. Sul, "New approach for high-performance PMSM drives without rotational position sensors," *IEEE Transactions on Power Electronics*, vol. 12, no. 5, pp. 904-911, 1997, https://doi.org/10.1109/63.623009.

[28] A. Apte, V. A. Joshi, H. Mehta and R. Walambe, "Disturbance-Observer-Based Sensorless Control of PMSM Using Integral State Feedback Controller," *IEEE Transactions on Power Electronics*, vol. 35, no. 6, pp. 6082-6090, 2020, https://doi.org/10.1109/TPEL.2019.2949921.

[29] J. Wang, Y. Liu, J. Yang, F. Wang and J. Rodríguez, "Adaptive Integral Extended State Observer-Based Improved Multistep FCS-MPCC for PMSM," *IEEE Transactions on Power Electronics*, vol. 38, no. 9, pp. 11260-11276, 2023, https://doi.org/10.1109/TPEL.2023.3279856.

[30] K. Choi, Y. Kim, S. -K. Kim and K. -S. Kim, "Current and Position Sensor Fault Diagnosis Algorithm for PMSM Drives Based on Robust State Observer," *IEEE Transactions on Industrial Electronics*, vol. 68, no. 6, pp. 5227-5236, 2021, https://doi.org/10.1109/TIE.2020.2992977.

[31] H. Liu and S. Li, "Speed Control for PMSM Servo System Using Predictive Functional Control and Extended State Observer," *IEEE Transactions on Industrial Electronics*, vol. 59, no. 2, pp. 1171-1183, 2012, https://doi.org/10.1109/TIE.2011.2162217.

[32] K. H. Kim, I. C. Baik, S. K. Chung and M. J. Youn, "Robust Speed Control of brushless DC Motor Using Adaptive Input-Output Linearization Technique," *IEE Proceedings - Electric Power Applications*, vol. 144, no. 6, pp. 469-475, 1997, https://doi.org/10.1049/ip-epa:19971428.

[33] A. Titaouine, D. Taibi, O. Bennis, F. Benchabane, R. Boumaraf and K. Yahia, "Adaptive nonlinear control combined with unscented Kalman filter for permanent magnet synchronous motor fed by AC/DC/AC converter," *International Aegean Conference on Electrical Machines and Power Electronics and Electromotion, Joint Conference*, pp. 26-31, 2011, https://doi.org/10.1109/ACEMP.2011.6490563.

[34] M. Ahrabi, S. Pradhan, S. Dhale and B. N. Mobarakeh, "Data-Based Model-Free Current Control of a PMSM Using Full-Form Dynamical Linearization Technique," *2023 IEEE Transportation Electrification Conference & Expo (ITEC)*, pp. 1-6, 2023, https://doi.org/10.1109/ITEC55900.2023.10187104.

[35] J. Ye, J. Yang, D. Xie, B. Huang and H. Cai, "Strong Robust and Optimal Chaos Control for Permanent Magnet Linear Synchronous Motor," *IEEE Access*, vol. 7, pp. 57907-57916, 2019, https://doi.org/10.1109/ACCESS.2019.2913900.

[36] Q. Li, X. Wang, J. Jiang, Q. Zhang and Q. Tong, "Sensorless control for surface mounted PM machine with a high inertial load," *CES Transactions on Electrical Machines and Systems*, vol. 2, no. 1, pp. 116-122, 2018, https://doi.org/10.23919/TEMS.2018.8326457.

[37] H. Lin, W. Yan, Y. Wang, B. Gao and Y. Yao, "Nonlinear sliding mode speed control of a PM synchronous motor drive using model reference adaptive backstepping approach," *2009 International Conference on Mechatronics and Automation*, pp. 828-833, 2009, https://doi.org/10.1109/ICMA.2009.5246257.

[38] H. Echeikh, M. A. Mossa, N. V. Quynh, A. A. Ahmed, and H. H. Alhelou, "Enhancement of inductionmotor dynamics using a novel sensorless predictive control algorithm," *Energies*, vol. 14, no. 14, p. 4377, 2021, https://doi.org/10.3390/en14144377.

[39] T. Takeshita and N. Matsui, "Sensorless brushless DC motor drive with EMF constant identifier," *Proceedings of IECON'94 - 20th Annual Conference of IEEE Industrial Electronics*, vol. 1, pp. 14-19, 1994, https://doi.org/10.1109/IECON.1994.397742.

[40] K. Ohnishi, N. Matsui and Y. Hori, "Estimation, identification, and sensorless control in motion control system," *Proceedings of the IEEE*, vol. 82, no. 8, pp. 1253-1265, 1994, https://doi.org/10.1109/5.301687.

[41] R. Wu and G. R. Slemon, "A permanent magnet motor drive without a shaft sensor," *IEEE Transactions on Industry Applications*, vol. 27, no. 5, pp. 1005-1011, 1991, https://doi.org/10.1109/28.90359.